Bulletin of Earthquake Engineering
https://doi.org/10.1007/s10518-026-02379-y

ORIGINAL ARTICLE

Evaluating damping schemes for the discontinuum seismic analysis of masonry cross-vaults

Yopi P. Oktiovan[1] · José V. Lemos[2] · Bora Pulatsu[3] · Francesco Messali[1] · Jan G. Rots[1] · Daniele Malomo[4]

Received: 8 July 2025 / Accepted: 22 January 2026

Abstract
Simulating the seismic behaviour of unreinforced masonry (URM) is challenging due to large deformations and severe damage. Capturing this highly nonlinear response requires advanced numerical modelling strategies that represent block separation, debonding, friction, and impact. Discontinuum-based modelling strategies, such as the Distinct Element Method (DEM), are well suited, as they explicitly represent bond failure and damage progression from cracking to collapse. DEM relies on the explicit time integration scheme of motion equations; hence, the choice of the damping scheme becomes critical. Typically, mass-proportional damping is used in dynamic analysis, often without complementing it with stiffness-proportional damping which requires unpractical reduction of the time steps to ensure numerical stability. Yet relying solely on mass-proportional damping can overdamp low frequencies and underdamp high frequencies. This study implements and validates an alternative damping approach, Maxwell damping, where multiple spring-dashpot elements are introduced at unit-mortar interfaces within a simplified micro-model. This work introduces an optimization algorithm to tune the Maxwell elements without heuristics, targeting near-uniform damping over a broad frequency range. Effectiveness is assessed against shake-table tests on a full-scale cross-vault URM specimen. Predicted displacements, accelerations, damage evolution, and computational efficiency is compared with mass-proportional and zero-viscous damping models. This study investigates Maxwell damping as a practical relaxation scheme for the seismic analysis of complex masonry systems using DEM, building on prior formulations in the literature and extending them to the present modelling and validation context.

Keywords Masonry cross-vault · Simplified micro-modelling · Distinct element method · Dynamic analysis · Rayleigh damping · Maxwell elements

Extended author information available on the last page of the article

Published online: 03 February 2026

1 Introduction

The seismic assessment of unreinforced masonry (URM) structures remains a significant challenge due to their inherent vulnerability to lateral loads and complex nonlinear behaviour under seismic excitations. Historical URM systems frequently incorporate intricate and curved geometries, such as cross-vaults, arches, and domes, which are prone to large deformations and exhibit highly nonlinear responses prior to collapse. Post-earthquake investigations (Sorrentino et al. 2014; Cole et al. 2012; Brandonisio et al. 2013) and analyses (Davis et al. 2023; D'Altri et al. 2017; Lagomarsino 2012) have consistently reported that masonry cross-vaults are particularly susceptible to earthquake damage due to the simultaneous activation of multiple collapse mechanisms. Depending on the direction of seismic excitation and interactions with adjacent structural components, out-of-plane collapse via four-hinge mechanisms and in-plane collapse due to vault web detachment may occur concurrently. Given this complex response, the development and validation of reliable numerical modelling strategies for URM cross-vaults have been a major focus of the research community in recent decades (Bertolesi et al. 2019). Among these, discontinuum-based numerical methods have gained prominence. These methods model masonry either at the microscale level, with individual units and joints represented explicitly, or at the mesoscale level, using blocky structures connected through zero-thickness interfaces defined by contact laws. The comprehensive review conducted by Malomo and Pulatsu (2024) highlighted the capabilities of discontinuum approaches for simulating various URM typologies under seismic loading, including (i) Joint opening/closure and frictional sliding; (ii) progressive bond failure and crack propagation without predefined paths; (iii) block separation, impact and pounding; (iv) out-of-plane (OOP) rocking, instability and overturning; (v) mechanism formation in walls and vaulted systems; and (vi) collapse at component and building scale.

Several discontinuum-based numerical methods have been employed for the seismic assessment of cross-vaults, including the Distinct Element Method (DEM) (Oktiovan et al. 2023b; Bianchini et al. 2024b; Mele et al. 2012), mixed FEM-DEM (Smoljanović et al. 2013), Non-smooth Contact Dynamics (NSCD) (Ferrante et al. 2024), and the Applied Element Method (AEM) (Davis et al. 2023). In this study, DEM has been selected for implementation due to its detailed modelling of individual components and its robust explicit time-marching integration scheme, which various researchers have already successfully employed ranging from simple geometries such as wall (Meriggi et al. 2019; Pulatsu et al. 2020; Oktiovan et al. 2024), arch (De Lorenzis et al. 2007; Lemos and Sarhosis 2023; Sarhosis et al. 2014), barrel vault (Oktiovan et al. 2023a; Chen et al. 2021), to complex geometries such as cross-vault (Davis et al. 2023; Oktiovan et al. 2023b; Bianchini et al. 2024), fan vault (Chen and Bagi 2024b), pavilion vault (Dell'endice et al. 2021), dome (Paris et al. 2020), buildings (Galvez et al. 2023; Malomo and DeJong 2022; Gubana and Melotto 2021), and many more.

Several authors have emphasized that the selection of damping schemes within DEM models can significantly influence the accuracy and computational efficiency of numerical analyses (Lemos and Sarhosis 2023; Lemos et al. 2022; Galvez et al. 2022a). In time-domain analysis, viscous damping models such as Rayleigh damping are frequently employed to account for dynamic energy dissipation not fully captured by constitutive hysteresis and contact mechanics. Rayleigh damping comprises two components, one proportional to the mass and the other to the stiffness of the mechanical system. However, Hall (2006)

and Galvez et al. (2022a), have cautioned that relying solely on mass-proportional damping can lead to unconservative or misleading collapse predictions due to spurious vibration damping and overfitting of damping parameters. Moreover, studies have shown that mass-proportional damping in DEM can result in unintended interface oscillations, particularly in curved geometries (DeJong 2009; De Lorenzis et al. 2007). On the other hand, using only the stiffness-proportional component can be computationally prohibitive, as it imposes very small timesteps for numerical stability. While stiffness-proportional damping has been shown to improve prediction accuracy for small-scale systems (Godio and Beyer (2019); Galvez et al. (2022b; Peña et al. 2007; Tomassetti et al. (2019)), its use in complex configurations such as cross-vaults remains impractical due to excessive computational demands.

To mitigate spurious high-frequency response without incurring severe timestep penalties, we adopt a Maxwell damping scheme (i.e., a generalized Maxwell/Maxwell–Wiechert model) in which linear Maxwell spring–dashpot branches are placed in parallel with the interface springs at unit–mortar contacts and with the internal tetrahedral elements of the deformable blocks. This yields a frequency-selective viscous dissipation akin to stiffness-proportional damping but without the severe timestep penalties, following Lemos et al. (2022); Lemos and Sarhosis (2023). The damping characteristics of the Maxwell scheme are optimised by tuning multiple elements simultaneously to achieve the desired damping ratio within a specified frequency band. Crucially, this paper introduces a novel optimisation framework that automatically calibrates the Maxwell parameters using a nonlinear least squares approach with the Levenberg–Marquardt algorithm. This eliminates the need for heuristic calibration or trial-and-error procedures, enabling a systematic and efficient search for optimal damping configurations (Lemos and Sarhosis 2023).

Various researchers have demonstrated the advantages of Maxwell elements as a dissipation mechanism in structural dynamics (Huang et al. 2019; Genta 2009; Liu et al. 1976). The effectiveness of the Maxwell damping scheme is benchmarked against mass-proportional, Rayleigh, and zero-viscous damping models. These schemes are evaluated in terms of their predictive accuracy and computational efficiency by comparing simulation results with shake-table test data of a masonry cross-vault subjected to unilateral seismic excitation (Bianchini et al. 2024a). Key performance indicators include displacement and acceleration time histories, damage patterns, and overall computational cost.

Building upon the foundational work of Galvez et al. (2022a) who examined damping schemes in the context of rocking simulations, as well as Lemos and Sarhosis (2023) who first applied Maxwell damping to small bi-dimensional URM components, this study makes a further advancement by applying Maxwell damping to a highly complex three-dimensional masonry structure. To the best of the authors' knowledge, this is the first study to integrate Maxwell damping with an optimisation algorithm for the dynamic analysis of a URM cross-vault using the DEM framework. The results provide critical insights into the application of DEM for nonlinear seismic assessment of intricate heritage structures and contribute to advancing damping strategies for improved predictive performance and efficiency.

2 Overview of the cross-vault shake-table experiment

To provide readers with appropriate context, this section briefly describes the experimental tests conducted by Bianchini et al. (2024a, b). Multiple researchers have also used the data from this experimental campaign as part of the Seismology and Earthquake Engineering Research Infrastructure Alliance for Europe (SERA) blind prediction and post-diction competition, summarized in the overview of the results by Calderini et al. (2024). The experimental campaign consists of incremental shake-table tests on two distinct configurations: an unstrengthened (UNS) specimen and a strengthened (STR) one with a steel/basalt grid and lime-based mortar. This paper focuses only on the unstrengthened case, which is used to evaluate all the numerical predictions obtained. The URM specimen was designed to represent a cross-vault located in a central aisle of a typical three-nave church (Bianchini et al. 2024a). The detailed specification of the specimen, along with the full-scale geometrical model, is presented in Fig. 1. The experimental specimens were constructed at LNEC, the National Civil Engineering Laboratory in Lisbon, Portugal.

The masonry cross-vault is a single-ring vault with a square plan of $3.5 \times 3.5\,\mathrm{m}^2$, a rise of 1.2 m, a net span of 2.9 m, and a thickness of 0.12 m. The specimen is placed on a $4.4 \times 4.9\,\mathrm{m}^2$ concrete slab, which is connected to the shake table actuator. The brick unit within the cross-vault was stacked in an orthogonal bond pattern with the unit dimensions of $0.045 \times 0.12 \times 0.23\,\mathrm{m}^3$ (H x W x L), and a 0.01 m thick mortar layer. Two movable piers of steel masses attached to wheels are left free to slide in both transversal and longitudinal directions. The other piers are made of masonry assemblages and are fixed to the reinforced concrete slab. To avoid torsional mechanisms, the piers are connected through three couples of $\phi 32$ mm steel bars, except for the fixed piers connection, which is done through steel profiles. Steel UPN profiles are also added to the fixed piers to increase the stiffness and reduce the relative displacements between the piers, as shown in Fig. 1. Four corners of the vault, up to half of its rise, have masonry infill, and steel profiles are added along the boundaries of the infill and the height of the steel supports for the fixed piers.

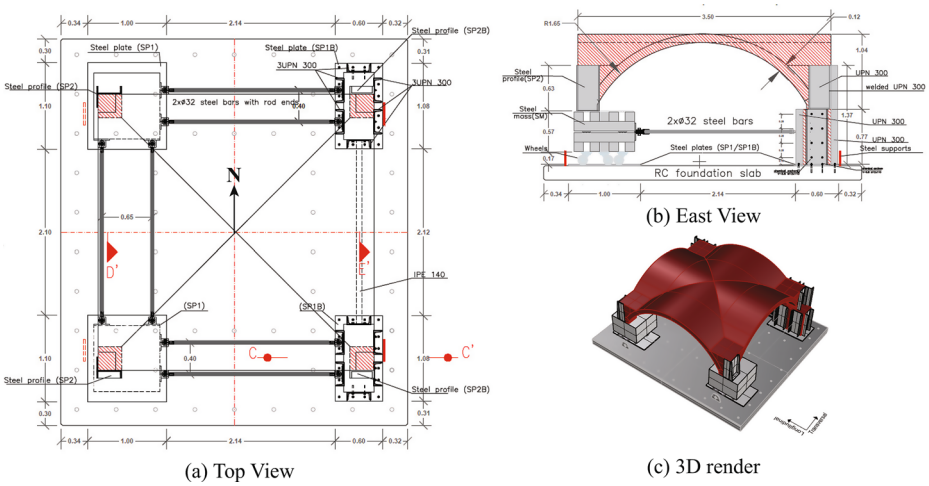

Fig. 1 The experimental cross-vault detailed specifications (Bianchini et al. 2024a)

The instrumentation setup for the UNS cross-vault specimen is shown in Fig. 2a. Four *optical cameras* (OC, i.e., still cameras used for optical displacement tracking) were placed to record the displacement response at the vault's extrados, following the experimental terminology of Bianchini et al. (2024a) (OC1–OC4; see Fig. 2a). Four video cameras (VC) on each elevation of the vault were used to document crack initiation and propagation during the tests

The seismic input is the 6th April 2009 L'Aquila earthquake record taken along the North-South direction from the Italian Rete Accelerometrica Nazionale (RAN) Station AQA (Bianchini et al. 2024a). Figure 2b illustrates the 75% scaled input (AQA75). The maximum absolute acceleration, velocity, and displacement of the AQA75 earthquake are $4.25\,\mathrm{ms}^{-2}$, $26.33\,\mathrm{cms}^{-1}$, and 37.0 mm, respectively. For the numerical analysis we adopt the 25 s input segment provided by the experimental campaign and use its first 15 s ($t = 0$–15 s) as loading. This truncation contains 97% of the Arias intensity of the 25 s sample (Fig. 2b). The effective duration based on the 5% to 95% Arias interval is 8.28 s.

The seismic load was applied unidirectionally along the longitudinal (North-South) direction of the vault four increments of amplitude considered for the UNS specimen; 10, 25, 50, and 75%. The shake-table test for the UNS vault specimen was performed up to the level of damage at which the structural equilibrium is still maintained, allowing strengthening through the TRM grid.

For more details regarding the material characterization tests, design and construction processes, and experimental results, readers are referred to Bianchini et al. (2024a). The experimentally observed crack patterns at the end of tests for 50 and 75% maximum amplitude of AQA EQ are presented in Fig. 3. No visible cracks were observed at the 10 and 25% load increments. At the end of 50% load increment, detachments between the infill masonry and the cross-vault were observed at both the fixed and moving piers in the north section (Fig. 3a). Significant damage was observed at the 75% load increment, representing an in-plane shear failure mode. The damage started from the vault crown, propagated toward the

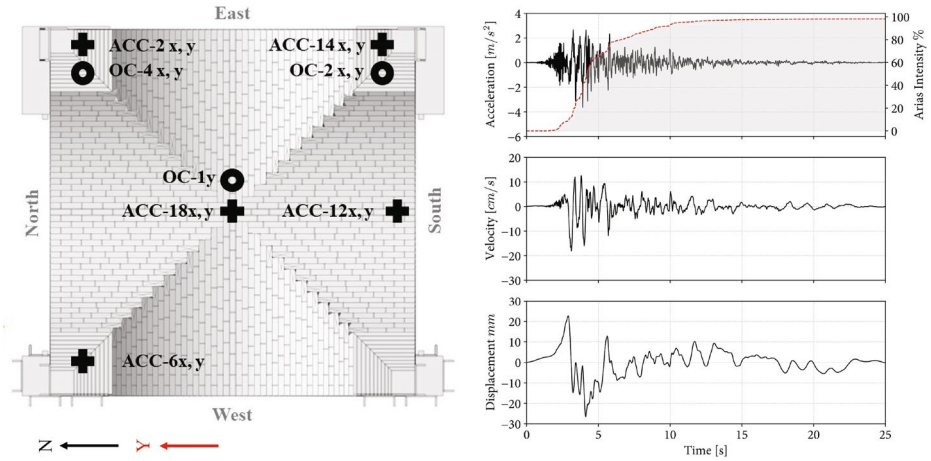

(a) Instrumentation setup (b) Input signals of AQA eq.

Fig. 2 Instrumentation setup of the unstrengthened (UNS) cross-vault specimen Bianchini et al. (2024a) and AQA75 input signal

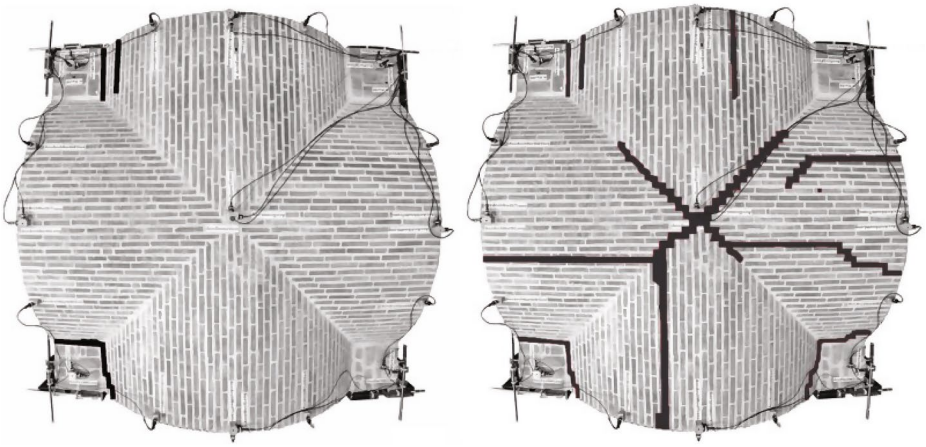

(a) AQA50 (b) AQA75

Fig. 3 Experimental crack patterns at the end of tests for 50% and 75% of AQA EQ amplitude Bianchini et al. (2024a)

groins in all directions, and eventually dispersed to the four webs of the cross-vault. Since full collapse was out of the scope of the experiment, load increment was stopped at 75%.

3 Distinct element modelling of masonry cross-vaults

This section provides an overview of the formulation adopted for the dynamic analysis using the Distinct Element Method (DEM), with particular focus on the numerical model developed for the cross-vault structure. The modelling approach, assumptions, and key parameters used in the DEM simulation are outlined, alongside a detailed description of the cross-vault geometry and contact definitions.

3.1 Formulation overview of the distinct element method

The modelling of the masonry cross-vault follows the principle of the simplified micro-modelling strategy, originally proposed by Lourenço and Rots (1997) and later simply defined as "meso-modelling" in discontinuum domains by Malomo and Pulatsu (2024), in which the unit-mortar nonlinearity is lumped at the zero-thickness interfaces formed between the contacting blocks, and the masonry units are extended to include the thickness of the mortar layers. A contact-based approach developed within the DEM scheme is implemented for the numerical analysis of the cross-vault model, as illustrated in Fig. 4. This approach represents the unit-mortar interfaces as assemblages of cohesive-frictional contact points (CPs) comprising three orthogonal springs (two in shear and one in normal directions). The extended masonry units are modeled as deformable blocks discretized into constant-strain tetrahedra with three degrees of freedom at each node. As the relative distance between two blocks falls within the specified tolerance of a fictitious plane (termed the common plane by Cundall (1988)) that bisects the contacting blocks, the blocks are assumed to be in con-

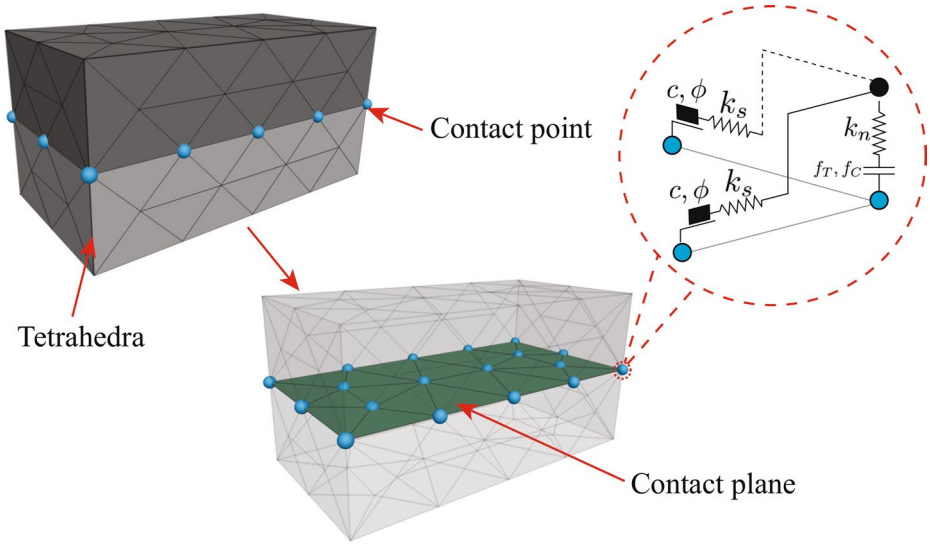

Fig. 4 Simplified micro-modelling strategy in DEM

tact, and the CPs are generated automatically. These CPs are then connected to the adjacent CPs generated within the common plane to create the interface, as shown in Fig. 4.

The equations of motion in DEM for static and dynamic problems are solved through an explicit time-marching integration scheme. This scheme is advantageous, particularly in the dynamic analysis of complex systems, as it allows continuous updates of the structural geometry and contact recognition as the simulation progresses, as well as finite (large) displacements and rotations of the blocks while maintaining the overall stability of the system. One drawback of the explicit solver is that small timesteps are needed to maintain numerical stability. The critical timestep is calculated in Eq. 1 (Lemos 2008), without considering damping.

$$\Delta t = \frac{2}{\omega_{max}} \quad \text{where} \quad \omega_{max} = \max\left(\sqrt{\frac{k_i}{m_i}}\right) \tag{1}$$

where m_i and k_i are the mass and stiffness associated with node i, respectively. The $\omega_{\max}$ term is an upper bound to the highest eigenfrequency of the linear elastic system, estimated with a conservative upper estimate of the stiffness to reduce the computational effort. For deformable block configuration with constant strain tetrahedral elements, the nodal stiffness k_i comprises both the stiffness of the element $k_{tet,i}$ and the contact stiffness $k_{n,i}$, where applicable (see Eq. 2 (Belytschko et al. 2013)).

$$k_i = k_{n,i} + k_{tet,i} \quad \text{where} \quad k_{tet,i} = \left(K + \frac{4}{3}G\right)\left(\frac{3A}{h}\right) \tag{2}$$

where K and G are the bulk and shear moduli, respectively, A is the largest tetrahedral area, and h is the shortest height of the tetrahedron. Finding a balance between the size of the tetrahedral elements (in terms of area and edge length) and their total number is essential for achieving an optimal stable timestep while maintaining the accuracy and efficiency of the numerical model. From Eq. (1)–Eq. (2), the stability controller is expressed in Eq. (3).

$$\omega_{\max} = \max_i \sqrt{\frac{k_i}{m_i}} = \max_i \sqrt{\frac{k_{n,i} + k_{\text{tet},i}}{m_i}} \tag{3}$$

For constant–strain tetrahedra, refining the mesh decreases the shortest height h (and typically increases the ratio A/h), which increases $k_{\text{tet},i}$ and hence $\omega_{\max}$. In addition, larger contact stiffnesses $k_{n,i}$ (when contacts are active) further raise k_i. Because the lumped nodal mass m_i scales with the element volume, the net effect of refinement is an increase in k_i/m_i, so that the critical explicit time step $\Delta t_{\text{crit}} = \frac{2}{\omega_{\max}}$ decreases with mesh refinement and with stiffer contacts. In practice, there is a trade–off between spatial resolution and computational cost. We choose the tetrahedral size such that the target frequency band is represented while keeping Δt_{crit} within feasible limits.

Energy dissipation in the dynamic analysis of masonry structures using DEM can be represented through viscous damping (e.g., Rayleigh or Maxwell damping), and the constitutive model of the contact points representing the unit-mortar interfaces, including frictional damping (Coulomb stick–slip dissipation) at the contacts. This paper investigates the dynamic behaviour of the cross-vault model with and without the presence of viscous damping. Different constitutive models are adopted depending on the contacting components to better represent the mechanical behaviour of the masonry and other components. The implemented contact constitutive model in the simulation of the cross-vault model is illustrated in Fig. 5 (Oktiovan et al. 2023b).

The elastic joint model (Fig. 5A) governs the interface behaviour through normal and shear stiffnesses, without incorporating any strength limits, and thus applies uniformly across all loading regimes. In the present setup, elastic joints are used for the auxiliary elements (backframe connectors and fixtures), where a linear elastic transfer of forces without inelastic mechanisms is intended. The Mohr–Coulomb joint model (Fig. 5B) builds upon the elastic formulation by introducing strength limits in tension (f_T) and shear $\tau_{\max}$, which degrade to the residual shear strength τ_{res} upon failure. We employ Mohr–Coulomb joints at the interfaces of the movable piers, where frictional strength and potential sliding govern the response.

The mortar joints in the discontinuum-based analysis of the cross-vault are modeled using the elasto–softening joint model (Fig. 5C), which provides a phenomenological representation of cracking, shearing, and crushing of masonry constituents through the unit–mortar interfaces Pulatsu (2023). This elasto–softening formulation is adopted for all masonry unit–mortar interfaces and for the infill-to-structure contacts, to capture tensile cracking, shear degradation, and compressive crushing. The fracture energies governing the post-peak behaviour in tension, shear, and compression regimes are defined empirically through Eq. (4) to (6), respectively Lourenço (2010).

$$G_f^I = 0.025(2f_t)^{0.7} \tag{4}$$

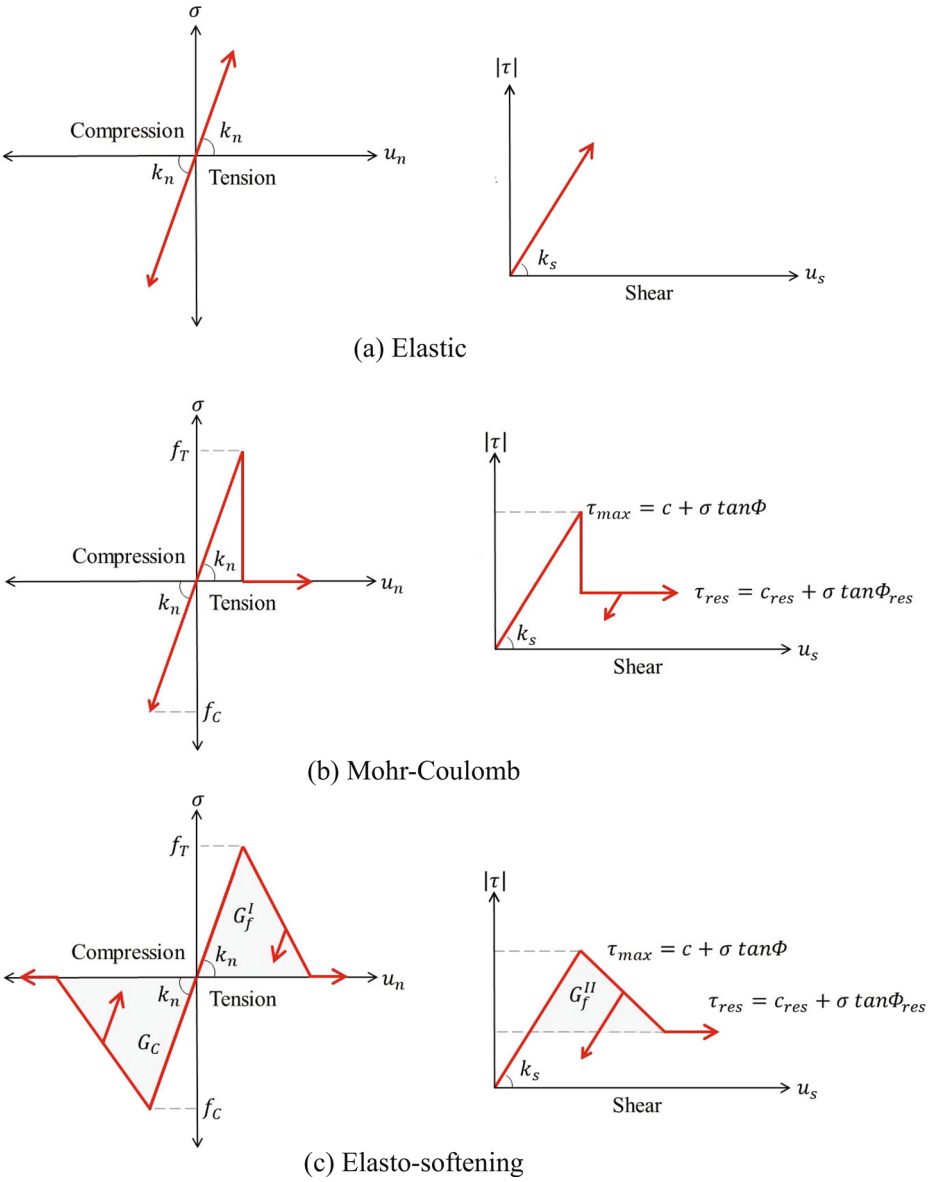

Fig. 5 Implemented contact model (Oktiovan et al. 2023b)

$$G_f^{II} = 10G_f^I \tag{5}$$

$$G_c = 15 + 0.43f_c - 0.0036f_c^2 \tag{6}$$

Equation (4) for Mode I and Eq. (6) for compression follow empirical relations reported in the CEB–FIP Model Code 1990 (CEBFIP1990 (1993)) for normal-weight concrete. Equation (5) adopts a common masonry-interface assumption used in micro/meso-modelling.

These expressions were originally devised for concrete and are used here by analogy for clay-brick masonry unit–mortar interfaces: parameters are reported in N/mm with strengths in MPa, and final values are calibrated to the target softening behaviour of the adopted elasto–softening joint law. This model also accounts for energy dissipation via hysteresis effects observed during unloading and reloading cycles. Contact stiffness degradation is considered in tension and compression for loading-unloading cycles, whereas the same initial stiffness is used upon unloading after peak strength in shear. Further details regarding the contact model can be found in Pulatsu (2023).

3.2 Description of the cross-vault numerical model

The cross-vault numerical model for this paper was taken from the work of Oktiovan et al. (2023b), from which the baseline model used in this work was taken and adapted according to the new scope of this paper. The model was built using COMPAS Masonry, an open-source computational framework for assessing unreinforced masonry structures (Iannuzzo et al. 2021). For details regarding the geometrical generation of the cross-vault model, readers are referred to Oktiovan et al. (2023b).

The mesh discretization of the cross-vault model in the DEM software *3DEC* (Itasca Consulting Group Inc 2013), utilized for the numerical analysis presented herein, is shown in Fig. 6a. The wheel system on the movable piers (Fig. 2) is disregarded in the numerical model due to modelling complexity. To allow the movable piers to slide along the horizontal directions, a significantly low shear stiffness and friction angle are applied to the contact points between them and the shake table base. As explained by Oktiovan et al. (2023b), movable piers and concrete foundation are meshed independently, considering different CST element edge-lengths to eliminate irregular meshes that could bottleneck the critical timestep of the system Eq.(1).

The maximum edge length for the tetrahedral elements of the masonry components is set to 25 cm while the maximum edge length for the steel frame and movable piers is set to 50 cm. The maximum edge length for the concrete elements (vault support, tie anchors, and shake table base) is set to 25 cm. The steel ties were also modeled using truss structural elements, with one degree of freedom at each end and a perfect connection to the tie anchors. The cross-section of the steel ties is $8 \times 10^{-4}\,\mathrm{m}^2$ and the density is set to $7800\,\mathrm{kg\,m}^2$. The contact discretization on each component of the cross-vault model is presented in Fig. 6b. The elastic joint model is defined for the contacts between the steel frame parts and the

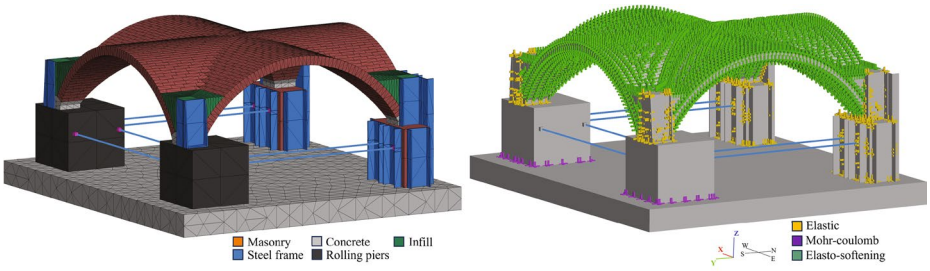

(a) Mesh discretization (b) Contact discretization

Fig. 6 Mesh discretization of the cross-vault components

Table 1 Material properties used for the modelling input parameters (Bianchini et al. 2024a)

Units		Mortar	Interface/joints			
Young's modulus[a]	Poisson ratio	Young's modulus[a]	Tensile strength	Comp. strength	Cohesion	Friction angle
[0.3 cm]E_b	v	E_m	f_t	f_c	c	ϕ
MPa	-	MPa	MPa	MPa	MPa	deg
6200	0.25	370.05	0.3	9.1	0.3	38

a Modulus of elasticity was obtained from the average slope of the secant line at 50% and 80% compressive strength

Table 2 Density and Young's modulus of the auxiliary components

Component	Density	Young's modulus	Poisson ratio
	ρ	E	v
	kg/m^3	GPa	-
Back Frame Steel	10685	200	0.3
Rolling Piers	5570	200	0.3
Tie Anchors	2000	200	0.3
Concrete	2000	25	0.3

other components. In contrast, the Mohr-Coulomb joint model with zero tensile strength, cohesion, and low friction is implemented on the movable piers to simulate the dry joint connection between them and the shake table base. The elasto-softening joint model is used to make contacts within the vault and infill components, better representing the mechanical behaviour of masonry constituents.

The material properties obtained from the material characterization test Bianchini et al. (2024a) and used as the modelling input parameters are summarized in Table 1. The normal and shear stiffnesses needed for the contact constitutive laws are obtained using Eq. (7) (Lourenço 1996)), where t_m is the thickness of the actual mortar layer. There is no distinction between parallel and perpendicular joints to the web of the vault in the cross-vault model for this paper.

$$k_n = \frac{E_b E_m}{t_m \left(E_b - E_m\right)} \quad \text{and} \quad k_s = \frac{k_n}{2(1+v)} \tag{7}$$

The normal and shear stiffnesses defined in Eq. (7) apply only to the brick-to-brick contacts, i.e., the contact points with the elasto-softening joint constitutive model. For the linear elastic joint model, the normal and shear stiffnesses are set to a relatively high value of $100\,\mathrm{GPa\,m^{-1}}$. For the Mohr-Coulomb joint model, the normal stiffness is set to $10\,\mathrm{GPa\,m^{-1}}$ to avoid interpenetration of the movable piers to the shake table base. The shear stiffness is equal to $0.01\,\mathrm{GPa\,m^{-1}}$ while the cohesive strength and friction angle are set to 0 MPa and 1°, respectively. Additionally, the density and Young's modulus of the auxiliary components are provided in Table 2. Since there are steel parts connecting the fixed piers, the density for the back frame is modified such that the numerical prediction error is negligible.

Density scaling is commonly used to enhance the computational efficiency of explicit solvers in the DEM, particularly for large and geometrically complex models (Malomo et al. 2019). In this approach, the density of certain elements is artificially increased to per-

mit a larger stable timestep, thereby reducing the overall simulation time. However, global density scaling—where the mass of all elements in the model is uniformly increased—can introduce significant inertial artefacts, making it unsuitable for dynamic simulations.

Nonetheless, small or highly distorted tetrahedral elements may still form during automatic mesh generation. These elements typically control the critical timestep due to their high stiffness-to-mass ratios, necessitating substantial timestep reductions to maintain numerical stability for the explicit integration scheme. To address this, partial density scaling is applied selectively to only the distorted elements. This localised adjustment increases their mass enough to meet a prescribed timestep, without significantly altering the system's total mass. In *3DEC*, the partial density scaling is applied by specifying a target timestep, allowing the program to apply the necessary amount of density scaling to the system to achieve that timestep.

The density scaling factor (dsf) shown in Fig. 7 is defined as a nodal mass multiplier, $\mathrm{dsf}_i = m_i^{\mathrm{scaled}}/m_i^{\mathrm{real}}$. Hence, $\mathrm{dsf} = 1.0$ indicates no mass scaling, while $\mathrm{dsf} > 1.0$ indicates added mass. Without applying partial density scaling, the critical timestep for the cross-vault model is limited to 5.27×10^{-7} s. By increasing the timestep to 1.25×10^{-6} s through partial density scaling, the total system mass increases by only 5.92%. Furthermore, as illustrated in Fig. 7, density scaling is confined to the steel components and tie anchors, which are not expected to influence the structural behaviour of the vault. Consequently, the numerical simulations presented in the following section employ density scaling with the target timestep of 1.25×10^{-6} s.

4 Damping for discrete dynamic problems

For solving dynamic problems using the Distinct Element Method, the numerical simulations should account for the forces required to stabilize the out-of-balance forces and the damping required to simulate the energy dissipation of the actual system when subjected to dynamic loading. In the case of dynamic analysis, viscous damping in the form of Ray-

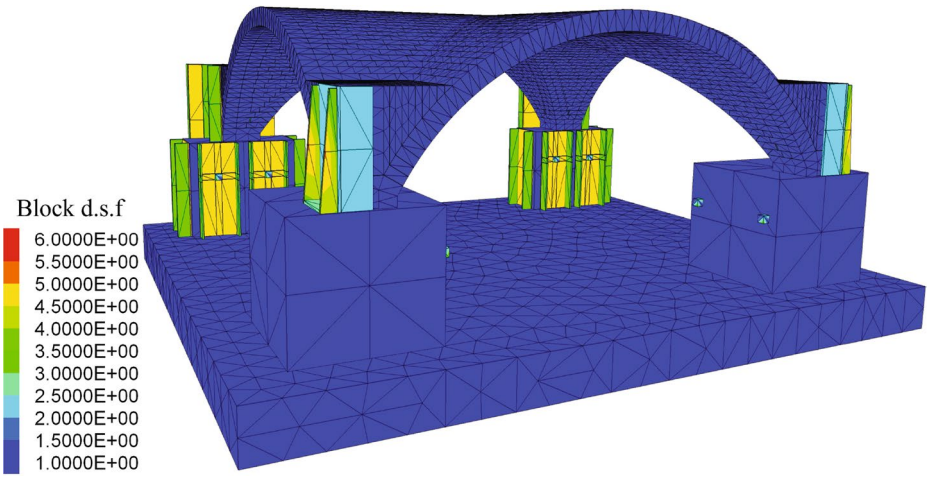

Fig. 7 Density scaling factor plot of the cross-vault model with the target timestep of 1.25×10^{-6} s

leigh damping formulation is typically used to dampen the oscillation of the system (Bathe and Wilson 1976), described in Sect. 4.1.The alternative damping scheme called Maxwell damping is implemented in this study, and the formulation is described in Sect. 4.2.

4.1 Rayleigh damping

Consider the equation of motion for a linear elastic multi-degree-of-freedom (MDOF) system, as shown in Eq. (8).

$$\mathbf{M}\ddot{u}(t) + \mathbf{C}\dot{u}(t) + \mathbf{K}u(t) = 0 \tag{8}$$

where M, C, and K are the mass, damping, and stiffness matrices, respectively, and $\ddot{u}(t)$, $\dot{u}(t)$, and $u(t)$ are the acceleration, velocity, and displacement vectors at time t. Rayleigh damping is defined as a linear combination of mass and stiffness matrices, expressed in Eq. (9).

$$\mathbf{C} = \alpha\mathbf{M} + \beta\mathbf{K} \tag{9}$$

where α and β are the mass-proportional and stiffness-proportional damping constants, respectively. The critical damping ratio ζ at any given angular frequency ω can be obtained as presented in Eq. (10).

$$\zeta_n = \frac{1}{2}\left(\frac{\alpha}{\omega_n} + \beta\omega_n\right) \tag{10}$$

The plot of the variation of the damping ratio towards the natural frequency is presented in Fig. 8. Aside from the Rayleigh damping variation from Eq. (10), the mass and stiffness components of the equation are also separated in Fig. 8. It can be seen that the mass-proportional damping provides a higher damping ratio at a lower frequency range, while the stiffness-proportional damps the higher frequency range. Several authors have utilized only the mass-proportional component of the Rayleigh damping for the dynamic analysis of masonry structures (Oktiovan et al. 2023b; Bianchini et al. 2024b; Masi et al. 2020; Galvez

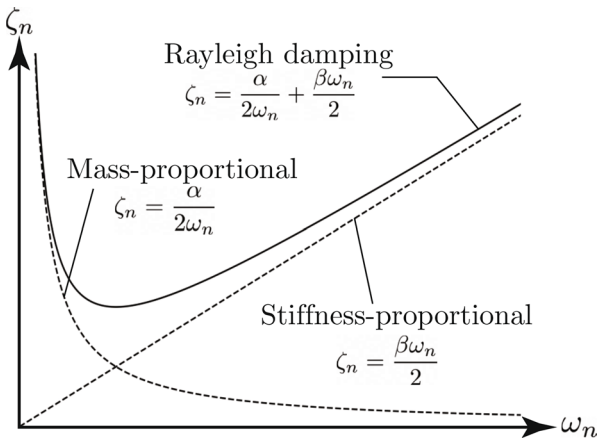

Fig. 8 Rayleigh damping and its components plot over natural frequency

et al. 2022b; Peña et al. 2007; Malomo and DeJong 2022; Kim et al. 2021; de Felice et al. 2022), successfully matching the numerical prediction against the experimentally observed values while disregarding the fact that the low-frequency range is overdamped and the high-frequency range is underdamped. Furthermore, the fundamental frequency of the numerical system at the damaged state could be reduced even further than the fundamental frequency at the undamaged state due to the progressive softening when nonlinear models are used. The damaged dominant frequency could fall into the low-frequency range for the mass-proportional damping in Fig. 8, resulting in an overdamped response at the failure or collapse condition of the numerical models.

On the other hand, due to the explicit time-marching integration scheme, the stiffness-proportional part of the Rayleigh damping is also discouraged in the DEM framework for analyzing complex masonry structures. Although the explicit algorithm for the DEM framework is sufficiently robust as it does not require matrix solutions and intricate techniques to deal with convergence issues, the algorithm is conditionally stable on the limiting timestep required to achieve stability (Eq. 1). With the stiffness-proportional damping considered, the limiting timestep is calculated according to Eq. (11) (Belytschko 1983).

$$\Delta t = \frac{2}{\omega_{max}} \left(\sqrt{1 + \zeta_{max}^2} - \zeta_{max} \right) \tag{11}$$

where $\zeta_{\max}$ is the critical damping ratio at $\omega_{\max}$. As the damping ratio increases linearly with the given frequency for stiffness-proportional damping (Fig. 8), the term in parenthesis in Eq. (11) causes a significant reduction to the limiting timestep Δt, up to one or two orders of magnitude (Lemos and Sarhosis 2023). The computational effort due to the timestep limitation could work under simple models or models with rigid block formulation. However, the reduction due to the stiffness-proportional component could be prohibitive in the complex cross-vault model with a deformable block configuration with many degrees of freedom.

4.2 Maxwell damping

Considering the limitation above on using Rayleigh damping for dynamic analysis, several researchers have used springs and dashpots placed in series to dissipate energy, termed the Maxwell element. Dawson and Cheng (2021) implemented a Maxwell damping formulation on finite elements using an explicit time-marching integration scheme for geotechnical seismic analysis. Lemos et al. (2022) implemented a similar formulation for the numerical analysis of rigid blocks using the DEM framework and extended the implementation for the dynamic analysis of masonry arches (Lemos and Sarhosis 2023). The Maxwell elements are applied in the joints between the blocks in DEM, as shown in Fig. 9. Maxwell spring–dashpot branches are attached in parallel to the internal tetrahedral elements of the deformable blocks, following the finite-element implementation of Dawson and Cheng (2021), where Maxwell branches are added in parallel to element stiffness and formulated in a modal/state-space form. This provides frequency-selective viscous dissipation with negligible change to the static elastic response. Dynamically, the added parallel stiffness produces only a small upward shift of natural frequencies and avoids the severe timestep penalties associated with stiffness-proportional Rayleigh damping.

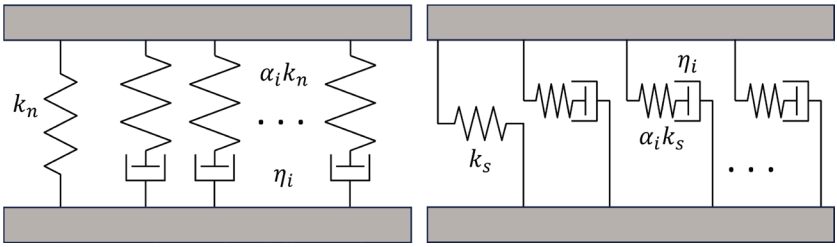

Fig. 9 Maxwell elements at the interface level

Through the joint constitutive model, the contact points relate the relative displacements and velocities between the blocks to the contact forces. The Maxwell elements are added in parallel with this joint constitutive model (represented in the forms of normal and shear springs in Fig. 9) and are subjected to the same relative displacements as the joint model.

4.2.1 Formulation for a single Maxwell element

The mathematical formulation for a single Maxwell element is hereby defined first. For simplicity, the mathematical formulation is explained in generic expressions that cover both the normal and shear directions. The Maxwell damping scheme concept is based on the Standard Linear Solid (SLS) model, which consists of two parallel systems: a Maxwell 'arm' with spring and dashpot in series and another system with only spring. The total joint stress in one contact point is the sum due to the joint constitutive model σ_j and the stress obtained from the Maxwell element σ^m.

The stress due to the constitutive model σ_j is a function of the elastic stiffness and the joint relative displacement under the linear elastic law. Meanwhile, the Maxwell element stress is explained in the standard visco-elastic equation (Findley and Davis 2013) where the joint displacement rate $\dot{u}$ is related to the Maxwell element stress σ^m and the stress rate $\dot{\sigma^m}$. The relation is defined in Eq. (12).

$$\dot{u} = \frac{\dot{\sigma^m}}{\alpha \cdot k} + \frac{\sigma^m}{\eta} \tag{12}$$

where α is the non-dimensional factor that defines the Maxwell spring as a fraction of the joint stiffness k, and the viscosity parameter η relates the joint stress to the joint displacement rate. The differential equation in Eq. (12) is solved in the frequency domain using the phasor method, where a steady–state harmonic motion is assumed and substituted to $u(t) = \Re\{\hat{u}\, e^{i\omega t}\}$ (and likewise for the internal variables), which yields the complex–amplitude relation summarized in Eq. (13). Note that, due to the viscous dashpot, stress and displacement are not in phase. In Eq. (13), u_0 and σ_0 denote the complex amplitudes (phasors) of displacement and stress, respectively.

$$u = u_0 \exp(i\omega t) \quad \text{and} \quad \sigma^m = \sigma_0^m \exp(i\omega t) \tag{13}$$

where ω is the angular frequency, u_0 and σ_0^m are the complex amplitudes of the displacements and Maxwell stress, respectively, which is governed by a complex modulus $k\overline{M}$, expressed in Eq. (14).

$$\sigma_0^m = k\overline{M}u_0 \quad \text{where} \quad \overline{M} = \frac{\alpha\tau^2\omega^2}{1+\tau^2\omega^2} + i\frac{\alpha\tau\omega}{1+\tau^2\omega^2} \tag{14}$$

where τ is the relaxation time, the ratio of viscosity η to elastic stiffness $k_M = \alpha k$. Since the SLS model comprises the Maxwell component and the elastic spring that acts in parallel, the stiffness of the SLS system is simply the sum of the individual stiffness. Therefore, the normalized complex modulus is given by Eq. 15.

$$\overline{M_T} = 1 + \overline{M} = 1 + \frac{\alpha\tau^2\omega^2}{1+\tau^2\omega^2} + i\frac{\alpha\tau\omega}{1+\tau^2\omega^2} \tag{15}$$

The critical damping ratio for the SLS model is then defined as the ratio of the imaginary and the real terms of the complex modulus (Dawson and Cheng 2021; Bland 2016), presented in Eq. (16). The critical damping ratio reaches the maximum value $\zeta_{\max}$ at the frequency of $\omega_{\max}$, as expressed in Eq. (17).

$$\zeta = \frac{\mathrm{Im}(\overline{M_T})}{2\mathrm{Re}(\overline{M_T})} = \frac{\alpha\,\tau\,\omega}{2\left[1+(\tau\omega)^2(1+\alpha)\right]} \tag{16}$$

where

$$\zeta_{max} = \frac{\alpha}{4\sqrt{1+\alpha}} \quad \text{at} \quad \omega_{max} = \frac{1}{\tau\sqrt{1+\alpha}} \tag{17}$$

The spring in the Maxwell element increases the overall stiffness of the joint, which is represented by the absolute value of the complex modulus, as shown in Eq. (18). At low excitation frequencies ($\omega \to 0$), the dashpots do not resist (their stress tends to zero), so the effective stiffness is that of the main elastic springs alone. At high frequencies ($\omega \to \infty$), the dashpots behave as rigid links (no dashpot deformation), and the effective stiffness tends to the sum of the main spring and all Maxwell-branch springs. At intermediate frequencies, the dashpots deform and carry stress, dissipating energy and yielding a nonzero damping ratio $\zeta(\omega)$.

$$|\overline{M_T}| = \sqrt{1+\alpha(2+\alpha)\frac{\tau^2\omega^2}{1+\tau^2\omega^2}} \quad \text{where} \quad |\overline{M_T}|_{max} = 1+\alpha \tag{18}$$

4.2.2 Formulation for multiple Maxwell elements

The general case for the Maxwell damping scheme comprises multiple Maxwell elements stacked in parallel along with the joint stiffness, as shown in Fig. 9. The Maxwell elements

are subjected to the same joint displacements, and the contact stress is calculated as the sum of the joint stress and all of the Maxwell element stresses. Figure 10a shows the plot of the damping ratio of each element Eq. (16) as a function of frequency, for a target damping ratio of 4% in the range 1 Hz to 40 Hz. The combined damping ratio (red curve in Fig. 10a) is obtained through the ratio of the imaginary and real components of the total complex modulus from multiple Maxwell elements, as shown in Eq. (19) for n Maxwell elements. Lemos and Sarhosis (2023) and Dawson and Cheng (2021) have shown that using three Maxwell elements is enough to provide a uniform damping over a range of frequencies. It is evident from Fig. 10a that the damping ratio is relatively uniform within the specified range of frequencies while gradually decreasing outside of that range.

$$\zeta_n = \frac{\mathrm{Im}(\overline{M_{T_n}})}{2\mathrm{Re}(\overline{M_{T_n}})} \quad \text{where} \quad \overline{M_{T_n}} = 1 + \sum_{i}^{n} (\overline{M})_i \tag{19}$$

Similar to the SLS model with a single Maxwell element, the magnitude of the total complex modulus in Eq. (19) imposes an increase in the joint stiffness due to the presence of the Maxwell elements. The plot of the magnitude of the total complex modulus at any given frequency is shown in Fig. 10b. The increase in the system's response frequency is proportional to the square root of the total modulus factor (Lemos and Sarhosis 2023). In the case of the three Maxwell elements in Fig. 10a and the corresponding dynamic modulus in Fig. 10b, the modulus reaches a maximum value of 1.39, which means that the Maxwell damping with three elements will impose an increase of approximately 1.18 in the upper-bound of the frequency range. The stiffness increase also causes a reduction of timestep in the explicit solver (Lemos and Sarhosis 2023), as presented in Eq. (20). The term in parentheses is the reduction of timestep imposed by the Maxwell damping scheme, with the sum of the α parameters representing the stiffness increase. The reduction due to Maxwell damping is smaller than Eq. (11).

$$\Delta t < \frac{2}{\omega_{max}} \left(\frac{1}{\sqrt{1 + \sum_i^n \alpha_i}} \right) \tag{20}$$

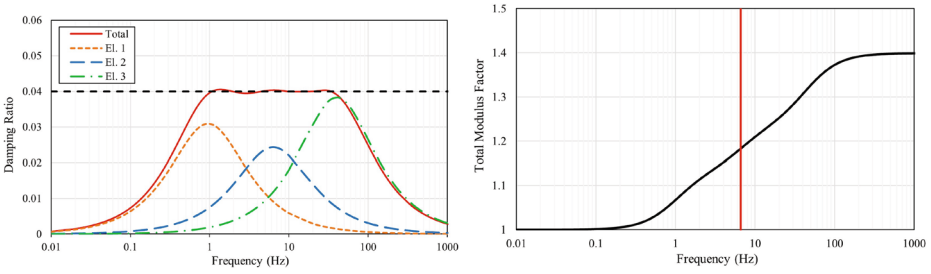

(a) Damping ratio (b) Magnitude of the total complex modulus

Fig. 10 Plot of damping ratio and magnitude of the total complex modulus vs input frequency for three Maxwell elements

The Maxwell damping elements are deactivated at the onset of tensile and shear failure, similar to the procedure used in stiffness-proportional damping, as the stiffness-proportional β component is implemented directly into the joint model.

4.2.3 Optimization algorithm for Maxwell damping parameters

While center frequencies and damping ratios can be tuned by trial-and-error (as in prior uses of Maxwell damping, e.g., (Lemos et al. 2022; Lemos and Sarhosis 2023; Dawson and Cheng 2021)), this work determines them by solving a nonlinear least-squares optimization problem that targets an approximately constant damping ratio $\zeta^\star$ over a specified frequency range $[\omega_{lb}, \omega_{ub}]$. To that end, a set of M=500 logarithmically spaced evaluation frequencies is sampled within the prescribed band:

$$\omega_j = \omega_{\mathrm{lb}} \left(\frac{\omega_{\mathrm{ub}}}{\omega_{\mathrm{lb}}} \right)^{\frac{j-1}{M-1}}, \quad j = 1, \ldots, M, \tag{21}$$

and the Maxwell parameters are identified by minimizing Eq. (22).

$$\min_{\{\alpha_r, \tau_r\}_{r=1}^{3}} \sum_{j=1}^{M} \left[\zeta^\star - \zeta(\omega_j; \boldsymbol{\alpha}, \boldsymbol{\tau}) \right]^2 . \tag{22}$$

where $\boldsymbol{\alpha} = \{\alpha_1, \alpha_2, \alpha_3\}$ and $\boldsymbol{\tau} = \{\tau_1, \tau_2, \tau_3\}$. To enforce bounds and ordering on the branch center frequencies without inequality constraints, unconstrained variables $\nu_k \in \mathbb{R}$ are mapped to strictly ordered scalars $t_r \in (0, 1)$ via Eq. (23).

$$t_r = \sigma(\nu_r) \prod_{k=1}^{r-1} [1 - \sigma(\nu_k)], \quad r = 1, 2, 3 \tag{23}$$

with $\sigma(u) = (1 + e^{-u})^{-1}$. Center frequencies are then set by a log–linear map on the prescribed band in Eq. (24).

$$\omega_r \; = \; \omega_{\mathrm{lb}}^{\,t_r} \, \omega_{\mathrm{ub}}^{\,1-t_r}, \qquad r = 1, 2, 3, \tag{24}$$

Enforcing Eq. (24) follows that:

$$\omega_{\mathrm{lb}} \; \leq \; \omega_1 \; < \; \omega_2 \; < \; \omega_3 \; \leq \; \omega_{\mathrm{ub}}. \tag{25}$$

Frequencies outside $[\omega_{\mathrm{lb}}, \omega_{\mathrm{ub}}]$ are not sampled and not part of the objective. The input parameter for the optimization algorithm is thus constrained to the target damping ratio $\zeta^\star$, and the frequency band $[\omega_{\mathrm{lb}}, \omega_{\mathrm{ub}}]$. The initial guess for the damping parameters at each Maxwell element is arbitrarily defined.

The objective in Eq. (22) is solved as nonlinear least squares with the Levenberg–Marquardt (LM) algorithm. Unless stated otherwise, equal weights are used, a gradient (infinity-norm) tolerance of 10^{-9} is adopted, and the maximum number of iterations is set to 200.

Initial values place ω_r uniformly on the log scale in $[\omega_{\mathrm{lb}}, \omega_{\mathrm{ub}}]$. Up to three small random restarts are allowed, and the best solution is retained.

The fitted damping curve is compared against the parameters reported by Lemos and Sarhosis (2023). For this comparison, the frequency band is set to 1 Hz to 40 Hz and the target damping ratio set to 5%, matching Lemos and Sarhosis (2023), while the initial guesses of the damping ratios for the three Maxwell branches are randomized. Figure 11 plots $\zeta(\omega)$ for the initial guess (green), the LM-converged fit (red), and the reference parameters from Lemos and Sarhosis (2023) (blue). In the case shown, convergence is achieved in eight LM iterations, and the fitted parameters reproduce the nearly uniform target damping within the specified band to a high degree of accuracy. The same optimization setup (band, grid, solver, and mappings) is used in all subsequent numerical analyses.

The Maxwell damping is assigned per contact point (and per internal tetrahedral link for deformable blocks), with three parallel Maxwell branches at each contact. Consequently, the formulation is mesh-agnostic as refining the discretization only changes the number of contacts, not the damping law at a contact. The parameter identification in Eq. (22) is also independent of mesh size and contact count. It fits dimensionless branch fractions and branch center frequencies/relaxation times to realize an approximately constant $\zeta(\omega)$ over a prescribed band, and the resulting three-branch set is applied uniformly to all contacts. If a change in discretization alters the model's resolvable frequency band (through $\omega_{\max}$ or numerical dispersion), the same optimization is re-run with the updated $[\omega_{\mathrm{lb}}, \omega_{\mathrm{ub}}]$.

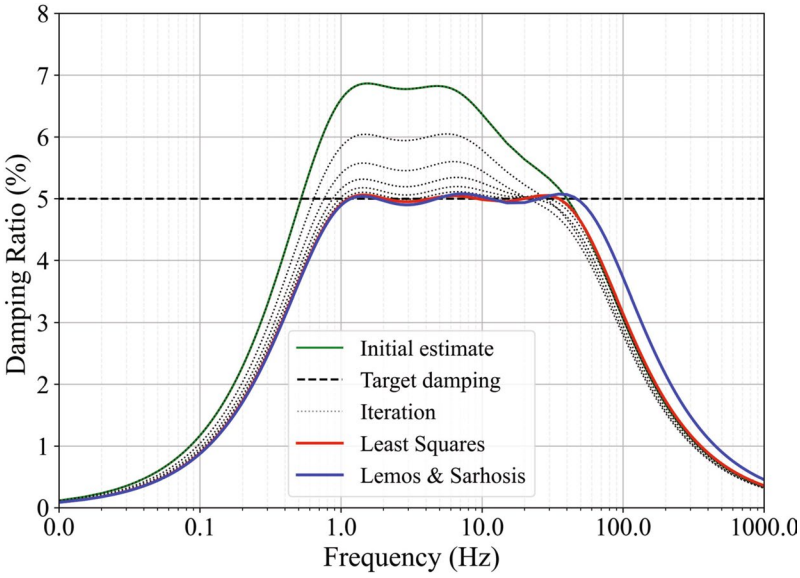

Fig. 11 Comparison of the Levenberg-Marquardt predicted Maxwell damping parameters against those reported by Lemos and Sarhosis (2023)

5 Comparison of damping schemes for seismic analysis - significant duration method

For the numerical analysis a fixed time window $t = 0$–15 s is used, extracted from the 25 s sample of the ground–motion record. This window contains 97% of the Arias intensity of that 25 s sample (the effective duration based on the 5–95% interval is 8.28 s). Due to the extremely small timesteps required by the stiffness-proportional and Rayleigh damping schemes—4×10^{-10} s and 5×10^{-9} s, respectively—even when partial density scaling is applied, the computational cost of performing a complete incremental dynamic analysis for the cross-vault model is prohibitively high. Consequently, in this section, the performance of the Maxwell damping scheme is evaluated only against the experimental results and benchmarked against the mass-proportional (MassProp) and zero viscous damping (noDamp) schemes. The plot of damping ratio over the frequency range for the MassProp and Maxwell models is shown in Fig. 12. It is important to highlight that noDamp model refers to the absence of viscous damping (e.g. Rayleigh or Maxwell damping), while the hysteretic damping is still present through the joint constitutive model.

The damping ratio for the MassProp model is taken at 4% with a center frequency of 7.5 Hz. The center frequency corresponds to the first mode natural frequency of the cross-vault model, which is slightly shifted to account for the reduction of the natural frequency due to damage. Meanwhile, the damping for the Maxwell model is set to 3% with a frequency range of 1 Hz to 40 Hz. The damping ratio is taken according to the previous prediction made by Oktiovan et al. (2023b) and suggestions provided by other researchers for masonry structures Bianchini et al. (2024b). The performance of each damping scheme is compared through the displacement and acceleration responses and damage patterns. All

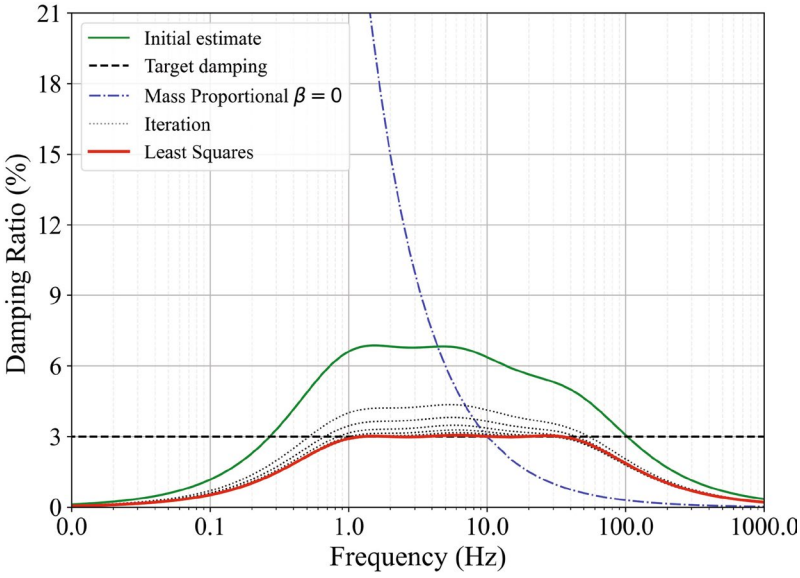

Fig. 12 Plot of critical damping ratio over frequency for mass-proportional damping and Maxwell damping

numerical models were conducted sequentially on a workstation with a Ryzen Threadripper Pro 5945WX processor (12-cores 4.1 GHz) and 256 GB of memory, on 3DEC v7.0.160.

To reduce bias from the damping parameters selection, a focused sweep was perormed around the selected damping parameters for both the MassProp and Maxwell models. For MassProp, target ratios $\zeta^* \in \{2, 3, 4, 5\}\%$ and center frequencies $f_c \in \{3,\ 7.5,\ 15\}$ Hz were tested. The target ratios were selected based on common practice for masonry structures, covering the accepted light-damping range for masonry with 5% as the code-reference spectrum (CEN 2004) and 2% to 5% as the commonly adopted near-linear regime. Meanwhile, the center frequencies were selected to cover the dominant response band of the undamaged and damaged states of the vault, with a simple octave spacing. This selection follows standard guidance for viscous damping calibration in structural dynamics (Chopra 2017) where band that contributes the most to the structural response was tuned to avoid unrealistically low/high targets that the model cannot resolve reliably.

For Maxwell, branches were identified on the fixed band $[1, 40]$ Hz with $\zeta^* \in \{2, 3, 4, 5\}\%$. The $[1, 40]$ Hz band is the intersection of the input's dominant content with the model's resolvable spectrum. A much wider band (e.g., $[1, 4000]$ Hz) lie largely outside the numerically meaningful range for this DEM discretization. Results are summarized for a displacement/drift channel (OC1-y) and the acceleration channel (ACC18-y) at the vault crown in Fig. 13.

For MassProp, ACC18-y favors larger f_c and ζ^*, while OC1-y favors moderate values at $f_c = 7.5$ Hz and $\zeta^* = 4\%$. The balanced setting *MP:* $\zeta^* = 4\%$ at $f_c = 7.5\,Hz$ was retained for validation runs to keep drift bias small while avoiding excessive low-mode damping. For Maxwell on $[1, 40]$ Hz, ACC18-y improves with increasing ζ^*, while OC1-*y* shows the smallest bias at $\zeta^* \approx 3\%$. The balanced setting *Maxwell:* $\zeta^* = 3\%$ on $[1, 40]\,Hz$ was adopted, prioritizing displacement while keeping accelerations acceptable. The summary is given in Table 3.

5.1 Displacement predictions

Comparison of the displacement responses from each damping scheme along the North-South direction at the crown of the cross-vault (the OC1-y measurement point in Fig. 2a) is shown in Fig. 14 from AQA25 to AQA75. The comparison initially examines the vault crown, as significant damage was noted during the last dynamic run (AQA75), allowing for a direct comparison of the performance of the damping schemes. It is important to note that the experimental displacement response was initialized to zero by subtracting all values from the first entry. At the 25% seismic load increment, the response of all models is identical, even up to the end of the analysis. Beyond 10 s, the predicted displacement response deviated by 18% for the MassProp and Maxwell models, and 20% for the noDamp model, compared to the experimentally observed values. This is due to observable diagonal cracks along the connections between the infill and cross-vault bricks (Bianchini et al. 2024a), which closed under the self-weight of the vault at the end of the shock.

The behaviour is relatively similar at the 50% seismic load increment, where the maximum peak at the positive loading direction was predicted significantly well by all compared damping schemes. When the seismic load changes direction at the dynamic time of 4 s, which was triggered by a low-frequency high-amplitude acceleration as shown in Fig. 2b, the prediction of the MassProp and Maxwell model underestimated the experimentally

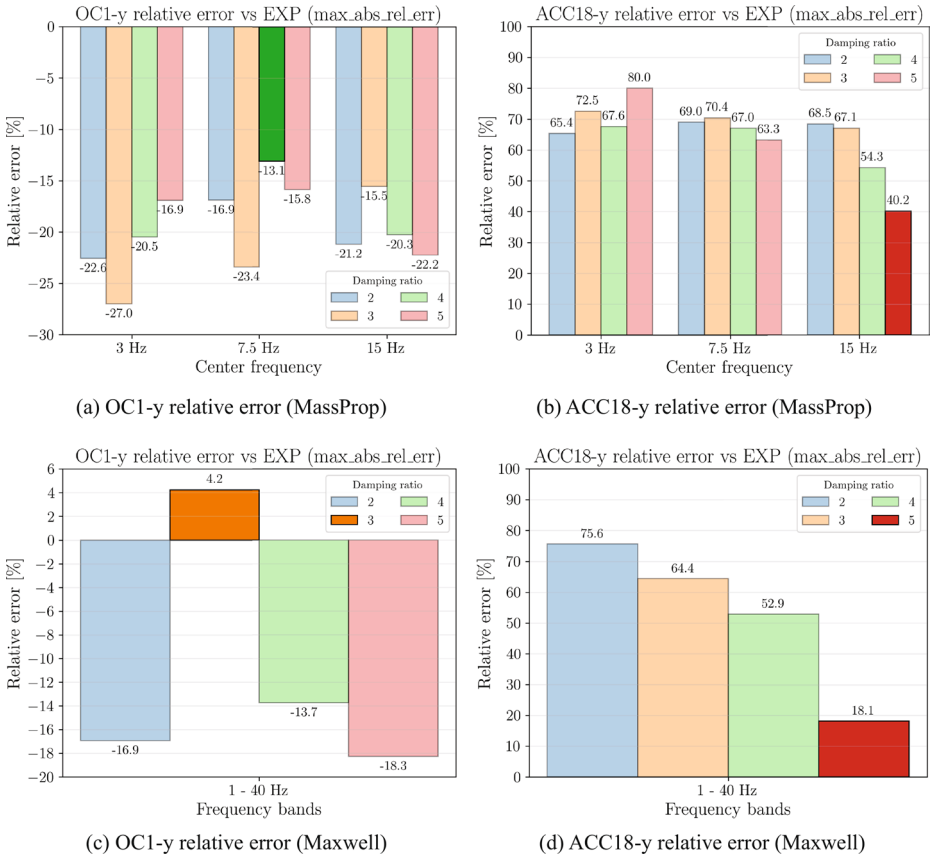

(a) OC1-y relative error (MassProp)

(b) ACC18-y relative error (MassProp)

(c) OC1-y relative error (Maxwell)

(d) ACC18-y relative error (Maxwell)

Fig. 13 Sensitivity analysis results for (**a-b**) MassProp and (**c-d**) Maxwell damping

Table 3 Sensitivity analysis: best cells vs. selected settings (signed peak bias, %)

Channel	Scheme	Best cell (grid)	Selected (validation)
ACC18-*y*	MP	5% @ 15 Hz: 40.2	4% @ 7.5 Hz: 63.3
OC1-*y*	MP	4% @ 7.5 Hz: −13.1	**4% @ 7.5 Hz: −13.1**
ACC18-*y*	Maxwell [1, 40] Hz	5%: 18.1	3%: 52.9
OC1-*y*	Maxwell [1, 40] Hz	3%: 4.2	**3%:** 4.2

observed response by 18%. This is due to the activation of frequency-dependent viscous damping on the mass-proportional and Maxwell damping schemes, in contrast to the sole presence of frequency-independent hysteretic damping in the noDamp model.

At 75% of the AQA eq., significant damage is observed at both the vault groins and webs as reported by Bianchini et al. (2024a). Similar to the previous seismic load increment, the peak displacement in the positive loading direction is predicted significantly well by all

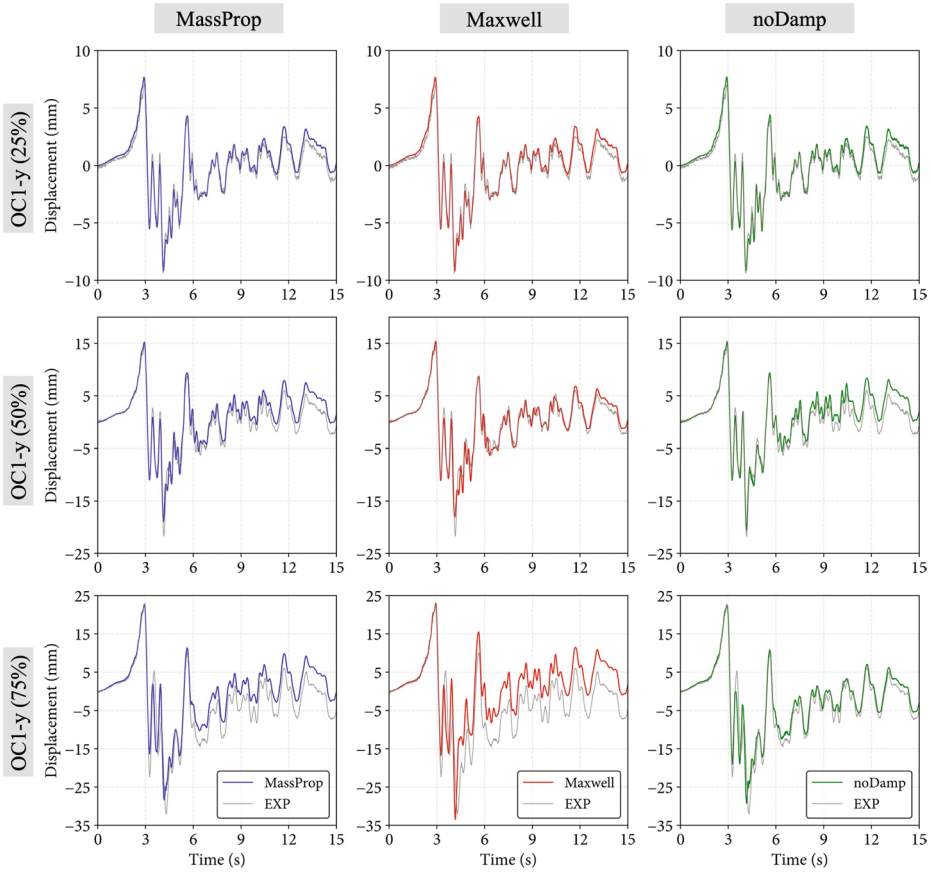

Fig. 14 Comparison of displacement response at the crown of the vault for each compared damping scheme

compared damping schemes. The seismic load that leads to the peak positive displacement (from time $t = 0$ s to 3 s) was the high frequency and relatively large amplitude, as presented in Fig. 2b. From time $t = 3$ s to 4 s, the seismic load input changes to a low-frequency and high-amplitude load. This transition to a low-frequency region causes the model with mass-proportional damping to overdamp the numerical model (Fig. 8). This results in the underestimated prediction of the negative peak displacement, as presented in the MassProp model with 75% load increment in Fig. 14.

In contrast, the Maxwell model predicts the peak displacement in the negative loading direction more accurately than the MassProp model, reducing the prediction error from 17% to 4%. The Maxwell damping does not overdamp the system's response as the seismic load input transitioned from high to low frequency with large amplitude due to the relatively uniform damping ratio applied from 1 Hz to 40 Hz. However, the model response after the peak displacement in the negative loading direction is relatively similar to that of the MassProp model, with the overall prediction error of 12% beyond 4.2 s. The only exception is that the

Maxwell model experienced higher fluctuation at the sudden change of loading direction from $t = 4$ s to 11 s.

Similar to the previous two models, the noDamp model predicts the positive peak displacement significantly well at the 75% increment of the AQA earthquake. The peak negative displacement is predicted with a 8% error, which is slightly better than the MassProp model but less accurate than the Maxwell model. This is postulated due to a more distributed failure of the joints found in the noDamp model compared to the MassProp and Maxwell models (Galvez et al. 2022a). As explained in the following section, the failure of the joints in the noDamp model is widely distributed along the web of the cross-vault in the North and West directions. The response of the noDamp model after the negative peak displacement is relatively similar to that of the MassProp model, with fewer fluctuations in the displacement response at the sudden change of direction, bringing the overall prediction error down to 4%. However, the displacement response after the negative peak displacement is closer to the experimentally observed values.

The prediction errors for the maximum (positive-peak) and minimum (negative-peak) displacements at all observed optical cameras (OC1, OC2, and OC4) are presented in Fig. 15a at the 75% of the AQA earthquake load. The locations of the optical cameras can be found in Fig. 2a. The comparison is done on the displacement parallel (North-South (NS), y) and perpendicular (East-West (EW), x) to the excitation direction. The displacement in the direction parallel to the seismic load is predicted relatively well, except for the OC_2 measurement point. Oktiovan et al. (2023b), Bianchini et al. (2024a, b) have reported that the OC_2 measurement point experienced a relatively large rotational effect that caused discrepancies in the displacement measurements (the maximum positive and negative displacements of NS and EW were observed between t equal to 10 and 14 s). From Fig. 15a, the cross-vault model with Maxwell damping can predict the experimental response slightly better than the MassProp and noDamp models. The prediction differences in the collapse state cannot be observed, as full collapse was beyond the scope of the experiment. Never-

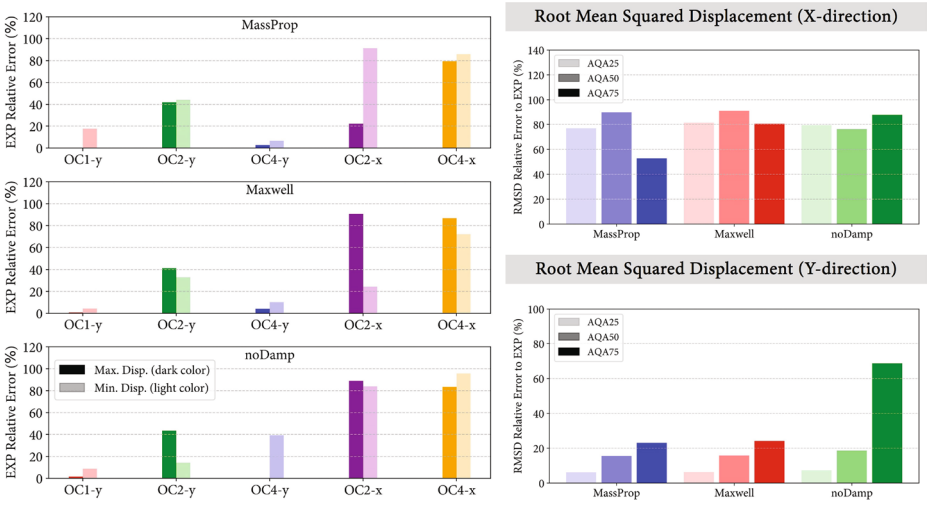

(a) Peak displacement relative error (b) Plot of the averaged NRMSE

Fig. 15 Displacement prediction error metrics relative to experimental values

theless, the relative errors of the absolute peak displacement on each damping scheme are 17.53%, 4.4%, 8.82% for the MassProp, Maxwell, and noDamp models, respectively. This shows that the Maxwell damping model is 75 and 50% more accurate than the MassProp and noDamp models, respectively.

To observe the deviation of the numerical prediction from the experimental value, the root mean squared displacement (RMSD) is calculated and compared against the experimental RMSD. Let $d \in \{x, y\}$ be the displacement in the East-West and North-South directions, respectively, $k \in \{1, 2, 4\}$ be the measurement point at OC_1, OC_2, and OC_4, and $\{t_i\}_{i=1}^{N}$ be the sampled times. For any signal $u^{k,d}(t)$ (both experimental and numerical), the RMSD is calculated as follows:

$$\mathrm{RMSD}^{k,d}[u] = \sqrt{\frac{1}{N}\sum_{i=1}^{N}\left(u^{k,d}(t_i)\right)^2} \tag{26}$$

Averaged across the selected optical cameras:

$$\overline{\mathrm{RMSD}}^{d}[u] = \frac{1}{3}\sum_{k=1}^{3}\mathrm{RMSD}^{k,d}[u] \tag{27}$$

which is then compared to the experimental RMSD to obtain the relative error:

$$\epsilon^{d}_{RMSD} = \frac{\left|\overline{\mathrm{RMSD}}^{d}[u] - \overline{\mathrm{RMSD}}^{d}[u_{exp}]\right|}{\overline{\mathrm{RMSD}}^{d}[u_{exp}]} \times 100\% \tag{28}$$

The averaged Normalized Root Mean Square Error (NRMSE) over the observed OCs is plotted in Fig. 15b. The deviation between the predicted displacement responses in the North-South direction for the MassProp and Maxwell models and the experimental responses increases as the applied seismic load increment rises. However, it is important to note that the relative error remains within 30% for both MassProp and Maxwell models. This finding is consistent with that of Bianchini et al. (2024b), where the numerically predicted displacement response also deviated at the 75% seismic load increment. The RMSD of the noDamp model experiences a sharp increase in the seismic increase 75% due to the significant deviation of the displacement response in $OC2y$ and $OC4y$, as presented in Fig. 16.

On the other hand, the predictions of all compared models along the East-West direction, for which displacement values are comparably smaller, deviate from the experimental responses even at the 25% of AQA earthquake load, even though the relative error drop for the MassProp and Maxwell model at the 75% seismic load increment due to the presence of failure at the masonry joints. These differences are due to multiple factors, including the large rotational effects found in the experimental measurement of $OC2$ and the opening of web joints close to $OC4$ at the 25% load increment reported in the experiment (Bianchini et al. 2024a). These factors are not primarily caused by the different viscous damping mechanisms applied to the numerical model. Furthermore, it is important to note that the displace-

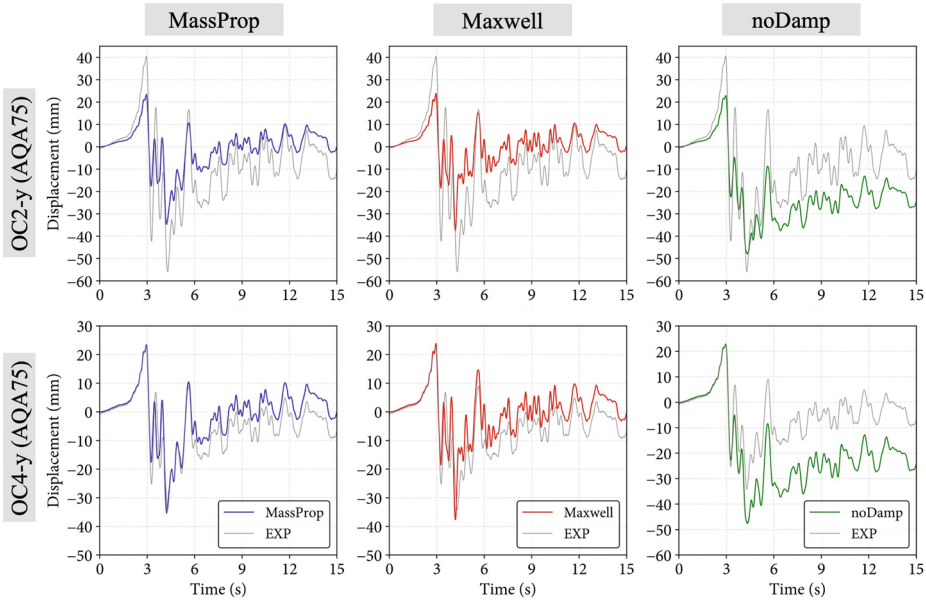

Fig. 16 Displacement response comparison of $OC2y$ and $OC4y$ at AQA75

ment response in the transverse direction is significantly lower than that of the longitudinal direction (maximum of 7.5 mm on $OC4x$ at AQA75 (Oktiovan et al. 2023b)).

Overall, the comparisons in Figs. 14 and 15a indicate good qualitative agreement between model predictions and measurements across the reported cases, with differences that are generally modest in amplitude and timing. Quantitatively, typical discrepancies are on the order of NRMSE $\approx 20\%$ for response histories and a peak drift error at $OC1_y$ of $\approx 20\%$. These figures should be interpreted as indicative rather than definitive: the number of test cases is limited and uncertainties in material properties and boundary conditions are non-negligible. Accordingly, the evidence supports the model's ability to reproduce key response features under the tested conditions but does not warrant strong general claims; broader datasets would be required to substantiate such claims. Finally, differences in the collapse state cannot be assessed here, as full collapse lay outside the scope of the experiment.

5.2 Damage pattern prediction

The numerically predicted damage patterns of the cross-vault model for each damping scheme at the end of each seismic load increment are presented in Fig. 17, with comparison to the experimental cracks in Fig. 3. The damage is viewed and compared only with the vault's extrados, as the experimental damage distribution was the most apparent and representative in this section. The damage pattern is obtained by plotting the scalar damage parameter based on the joint constitutive law proposed by Pulatsu (2023). At the 75% input level, the numerical response of all compared damping schemes is generally consistent with the experimental observation in Fig. 3b. Among them, the Maxwell configuration provides the closest qualitative match in terms of first-crack locations, hinge formation at

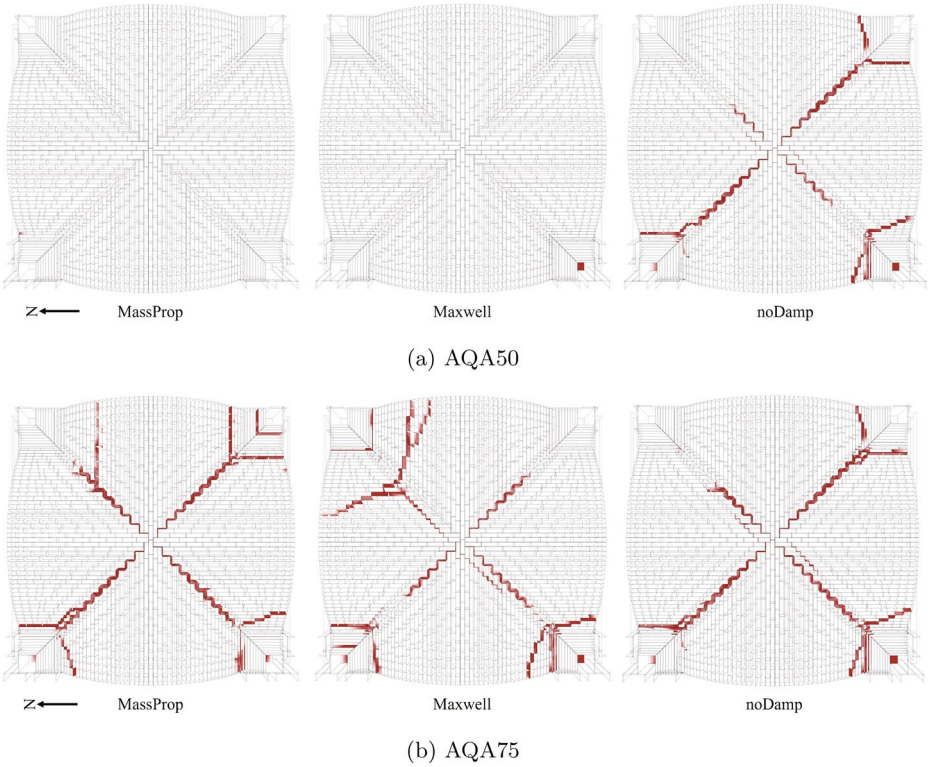

Fig. 17 Predicted damage pattern from the compared damping schemes at (**a**) AQA50 and (**b**) AQA75. Comparison is drawn to Fig. 3

the haunches, and overall damage extent, while the other schemes capture the same mechanisms with small differences in extent and localization.

At AQA25, all models show no relevant damage at the vault sections, consistent with the experimental response. At AQA50, the noDamp model suffers significant damage at the vault groins and connections to the infill elements. Failure at the Northern and Eastern webs is observed in the noDamp model (Fig. 17a). Meanwhile, only slight detachment is found at the northern web and the infill elements for the MassProp and Maxwell models. At AQA75 (Fig. 17b), the MassProp model exhibits detachment of the northwest and southeast piers with damage at the vault groin distributed in all directions. Damage through the web is observed in the eastern section of the vault, propagating from the vault groin. The Maxwell model also exhibits damage at the vault groin, which propagates in all directions, even though the intensity was visibly less compared to the MassProp model. The cracks in the Maxwell model, which propagate from the vault groin, are also found through the northern, eastern, and western webs. The difference between the MassProp model and the Maxwell model is that the Maxwell model does not exhibit infill element detachments in the southeast section of the vault. Furthermore, the cracks on the northeastern groin of the Maxwell model drift slightly and propagate through the adjacent vault webs instead. This is postulated due to the formation of the hinge line away from the vault crown.

Finally, the joints of the noDamp model damaged at AQA50 are propagated further at AQA75. The cracks at the vault groin are found in all directions of the groin, but the intensity was scattered, where the cracks in the northeastern groin are visibly lower than those in the other groins. Furthermore, detachments are observed in all connections between the infill and vault elements except for the northeast pier, followed by cracks propagating through the vault webs. Cracks propagating through the vault webs from the crown are observed in the noDamp model.

The noDamp configuration is used as a lower-bound damage-prone baseline: by excluding viscous damping, the model tends to anticipate crack initiations and propagations at earlier stages of the seismic loading (see Fig. 17a). While such early cracking cannot be entirely ruled out experimentally, especially for minor diagonal fractures, the measured sequence (Bianchini et al. 2024a) suggests that the time of occurrence and extent of diagonal cracking in the noDamp model are conservative relative to test observations. The close match of the noDamp displacement during the 0–6 s window of AQA50 (Fig. 14) reflects the system's response before substantial joint degradation has occurred. Beyond that, the lack of frequency-dependent damping leads to noisier accelerations and sustained oscillations, as shown in the next subsection.

Overall, the comparisons in Figs. 17 and 3 indicate that the model captures the primary features of the observed damage pattern (locations of first cracking, dominant shear slip along unit–mortar interfaces, and hinge formation at the vault haunches). Differences remain in crack extent and exact localization, which are sensitive to thresholding and registration of the experimental images as well as to uncertainties in joint parameters and boundary conditions. Given the limited number of tests and the qualitative nature of the available ground truth, these results should be viewed as indicative rather than conclusive. The figures are intended as the primary basis for comparison, and the observations support the model's ability to reproduce salient damage mechanisms under the tested conditions, without warranting strong general claims. A broader validation with additional specimens and independent damage quantification would be needed for firmer conclusions.

5.3 Acceleration predictions

Further comparison of the performance of the damping schemes includes analyzing the model's acceleration response compared to the data recorded by the accelerometers during the experiment. The experimental acceleration is determined by the accelerometers attached to the vault extrados. However, the acceleration response from the numerical model cannot be directly obtained, as the explicit solution procedure of the blocky system in *3DEC* typically produces excessive noise in the higher frequency range. Therefore, the model output is first recorded as translational velocities at the corresponding global X or Y direction at the node closest to the instrument location. Accelerations are then obtained by numerical differentiation of these velocities using a centered finite-difference scheme on a uniform time grid. These accelerations are then immediately compared to the experimental results. This allows an averaged acceleration response over the given time interval to be obtained.

The acceleration prediction at the vault crown for each damping scheme is shown in Fig. 18 at each seismic load increment. At 25% load increment, both MassProp and Maxwell models predict the acceleration response at the vault crown relatively well compared to the noDamp model. On the other hand, there is significant noise in the acceleration response of

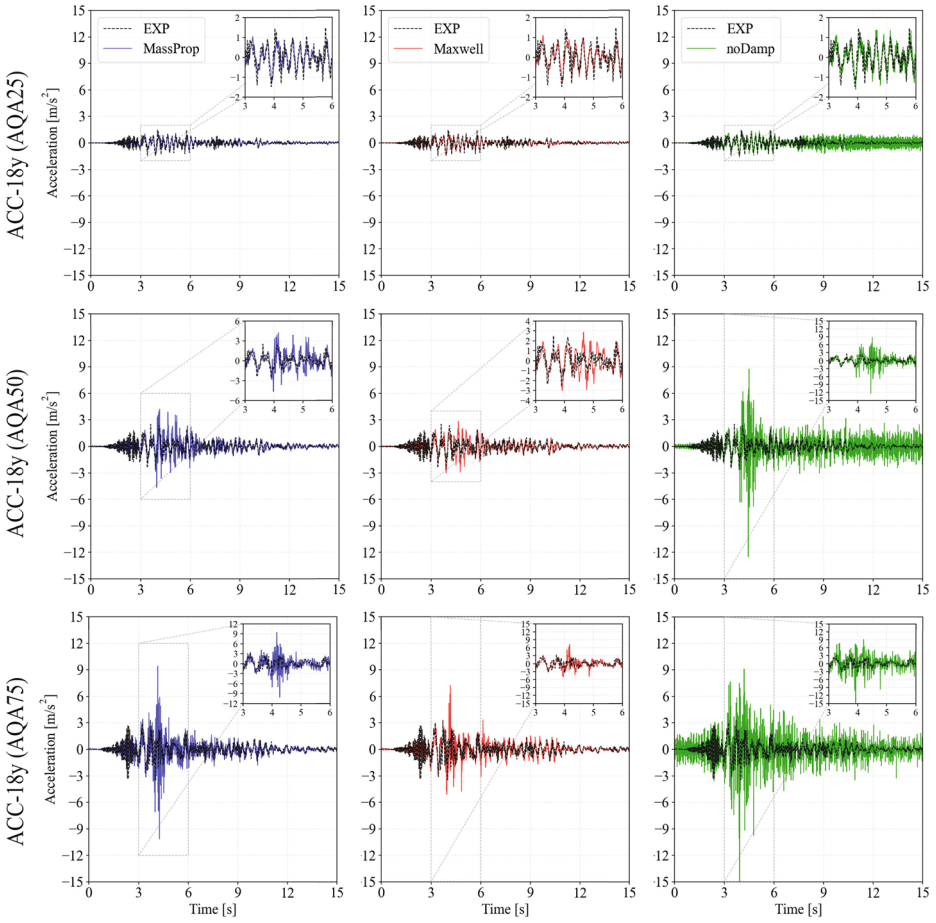

Fig. 18 Comparison of acceleration response at the crown of the vault

the noDamp model, specifically at the low frequency and high amplitude sequence from t equals 3 s to 4 s.

At 50% load increment, the acceleration response of MassProp and Maxwell is relatively similar. The difference lies in the slightly higher amplitude from 4 s to 5 s for the Maxwell model. Since the noDamp model experiences significant damage at the vault groins, the northern web, and the detachments of infill elements (Fig. 17a), the acceleration response is noisier compared to the 25% load increment. Furthermore, the acceleration response beyond 7 s shows a steady-state response which fluctuates between $-2.5\,\mathrm{m\,s^{-2}}$ and $2.5\,\mathrm{m\,s^{-2}}$. This highlights that frequency-independent hysteretic damping is often inadequate to dampen the numerical model properly when subjected to seismic load.

At 75% load increment, the acceleration response of all compared damping schemes is considerably different. The MassProp acceleration response shows high fluctuations at the low-frequency, high-amplitude sequence. This is the consequence of impacts in opening and closing contacts, which generate high-frequency noise in the velocity and acceleration responses. Since mass-proportional damping is applied to the equations of motion, it has a

more marked effect on rigid body motion than the impacts between the blocks in contact. It has to rely on the hysteretic damping through the contact constitutive model.

The cross-vault model with Maxwell damping, on the other hand, can dampen the high-frequency impact due to blocks in contact, as seen in the 75% load increment plot of the Maxwell model in Fig. 18. The acceleration response at the sequence between 3 s and 4 s is considerably lower compared to the MassProp model. Similar to the stiffness-proportional damping, the Maxwell damping is directly applied to the masonry joints, so the high-frequency impact caused by the opening and closing contacts can be damped more effectively. The response beyond 4 s is similar to that of the MassProp model, where the viscous damping and the equilibrium state of the cross-vault dampen the acceleration response.

The noDamp model response is also considerably different. As damage in the vault groin and the webs already existed at the previous load increments, it is clear that the model started with high fluctuations of acceleration response between 0 s and 2 s. The low-frequency and high-amplitude excitation do not significantly affect the acceleration response at the vault crown, as the joints are already opened in this state. The steady-state response beyond 4 s persists until the end of the analysis.

The numerical prediction of the other observed accelerometers in Fig. 2a is presented in Fig. 19 regarding the relative error of the maximum and minimum acceleration to the experimental values. Given experimental acceleration $a^{\mathrm{EXP}}(t)$ and numerical acceleration $a^{\mathrm{NUM}}(t)$, define the experimental extremes over the analysis window J as Eq. (29)

$$a^{\mathrm{EXP}}_{\max} = \max_{t\in J} a^{\mathrm{EXP}}(t), \qquad a^{\mathrm{EXP}}_{\min} = \min_{t\in J} a^{\mathrm{EXP}}(t), \tag{29}$$

and the numerical extremes $a^{\mathrm{NUM}}_{\max}$, $a^{\mathrm{NUM}}_{\min}$ analogously. The relative errors reported in Figure 19 are then defined as Eq. (30)

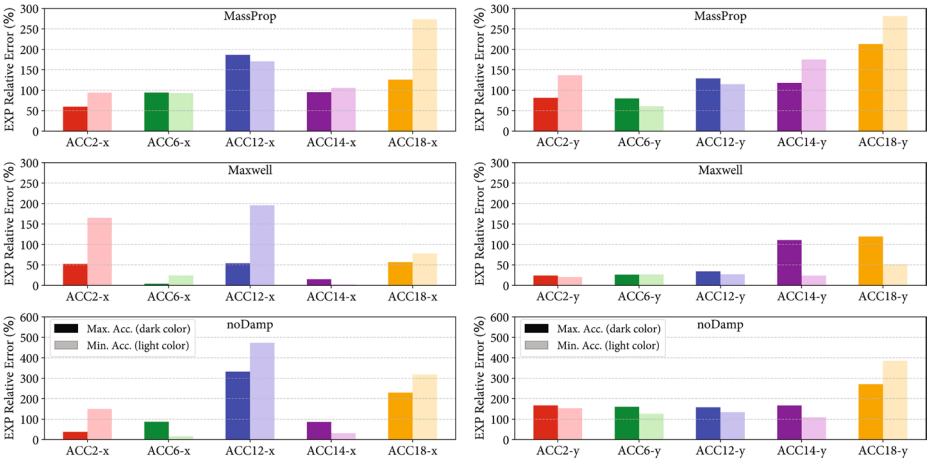

Fig. 19 Relative error of maximum and minimum accelerations (NUM vs. EXP). Dark bars: $\mathrm{RE}_{\max}$ (maximum acceleration); light bars: $\mathrm{RE}_{\min}$ (minimum acceleration)

$$\mathrm{RE}_{\max}[\%] = 100\,\frac{\left|\,a_{\max}^{\mathrm{NUM}} - a_{\max}^{\mathrm{EXP}}\,\right|}{\left|\,a_{\max}^{\mathrm{EXP}}\,\right|}, \qquad \mathrm{RE}_{\min}[\%] = 100\,\frac{\left|\,a_{\min}^{\mathrm{NUM}} - a_{\min}^{\mathrm{EXP}}\,\right|}{\left|\,a_{\min}^{\mathrm{EXP}}\,\right|}. \tag{30}$$

The acceleration responses in the X-direction (Fig. 19a) predicted by the Maxwell damping model agree relatively better with the experimental values than the MassProp and noDamp models. The Maxwell model overpredicts the Y-direction of the ACC14 and ACC18 accelerometers (Fig. 19b), corresponding to the southeast pier and vault crown, respectively. As previously observed at the measurement of OC-2, there was a large asymmetric movement at the southeast pier that persisted until the end of the experiment. This asymmetric rotational movement was not captured in any numerical model. Furthermore, the discrepancy found at ACC18 could be caused by the numerical artifacts, as extensive damage is observed at the vault crown. These numerical artifacts denote the spurious high-frequency content that can arise locally from rapid contact-state changes (stick-slip and open-close transitions) at the unit-mortar interfaces, mesh-dependent local modes of the tetrahedral blocks near the crown, and amplification introduced by numerical differentiation when computing the numerical accelerations. These effects are most pronounced near the vault crown (ACC18), where damage initiates and contact transitions are most frequent. On average, the Maxwell damping model predicts the acceleration responses 64.68% and 74.73% more accurately than the MassProp and the noDamp model, respectively.

In conclusion, even though predicting the acceleration responses of an experimental shake-table test is challenging for a numerical model with an explicit solver, using appropriate damping schemes could alleviate the difficulties by isolating the acceleration response due to numerical artifacts and the actual response due to the structure being subjected to excitations. It is also important to point out that solely hysteretic damping on seismic analysis is inadequate to dampen the steady state acceleration response, as shown in Fig. 18.

5.4 Required computational times

The total elapsed time of all models for each level of seismic input is summarized in Table 4. From the total elapsed time of the Maxwell model, it is evident that Eq. (20) imposes a slight reduction of the timestep required for numerical stability, which eventually causes an increase in the total elapsed time of the incremental dynamic analysis. In the case of the cross-vault model with Maxwell damping set at 3%, the total elapsed time is 50% longer than the model with mass-proportional damping set at 4%.

The noDamp model experiences a slight decrease of 8% in the total elapsed time compared to the MassProp model. This difference can be attributed to many factors, including the processors' performance and the variability in the complete mechanical cycle, which considers the total number of contacts, contact updates, calculation of internal stresses in the blocks, etc.

Table 4 Total elapsed time of all models divided for each level of seismic input

Model	dynamic timestep	AQA25	AQA50	AQA75	Total	Time reduction vs Maxwell
	[s]	[min]	[min]	[min]	[h]	[%]
MassProp	1.25×10^{-6}	1066.73	1057.00	1051.28	52.91	33.38
Maxwell	9.37×10^{-7}	1633.15	1611.70	1522.12	79.43	-
noDamp	1.25×10^{-6}	1066.73	909.48	935.63	48.53	38.90

6 Comparison of damping schemes for seismic analysis with wavelet-based truncation method

In the previous section, it was mentioned that conducting incremental dynamic analyses with complete input signals for the stiffness-proportional and Rayleigh damping schemes is complex due to the prohibitive timestep limitation (see Eq. (11)). This section presents modifications to the cross-vault model to facilitate the use of Rayleigh and stiffness-proportional damping schemes. However, even with these modifications, implementing stiffness-proportional damping for a large and complex model, such as the one simulating a cross-vault, is still significantly prohibitive. Therefore, this section exclusively compares responses from the Rayleigh damping (Rayleigh) scheme against the mass-proportional damping (Mass), Maxwell damping (Maxwell), and zero viscous damping (noDamp) schemes.

6.1 Modifications on the numerical model and seismic record

This sub-section introduces two modifications that help simplify the numerical model and therefore improve computational efficiency.

6.1.1 Mixed discrete-continuum modelling approach

First, as shown in Fig. 7, the steel frame elements are subjected to significantly higher levels of density scaling compared to the rest of the structure. This indicates that the smallest elements—those which govern the critical timestep of the system via the m_i term in Eq. (1)—are concentrated within the steel frame. To address this bottleneck, a mixed discrete–continuum modelling approach is adopted following Pulatsu et al. (2019). In this strategy, the steel frame is treated as an auxiliary structural component and modelled as rigid blocks, while the remainder of the structure is modelled using deformable blocks. Rendering the steel elements rigid not only eliminates their influence on the limiting timestep by removing their small deformable mesh size, but also reduces the overall geometrical complexity of the model. This simplification significantly increases the stable timestep, thereby improving the dynamic analysis's computational efficiency.

This allows the target timestep for density scaling to be increased from 1.25×10^{-6} s to 4.5×10^{-6} s with significantly less impact of the density scaling on the essential elements (e.g., vault, infill, or the pier elements). The mixed discrete-continuum model is then rerun with the same input signal used in Sect. 5. The comparison of the displacement response at the vault crown at each load increment is given in Fig. 20.

6.1.2 Wavelet-based truncation of the seismic record

Second, given the practical challenges in applying the same truncated input record used in Sect. 5 to models incorporating full Rayleigh damping, particularly the stiffness-proportional (SP) variant, an alternative truncation strategy is introduced to improve feasibility. For this purpose, the wavelet-based truncation method proposed by Repapis et al. (2020) is adopted. In this method, a single finite-duration pulse (termed the mother wavelet) of Mavroeidis–Papageorgiou (M&P) type Mavroeidis et al. (2004) is fitted to the processed velocity record. The MP pulse uses a cosine carrier under a raised-cosine envelope

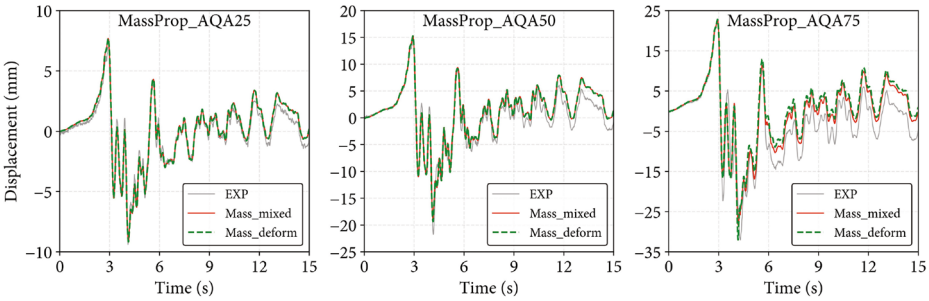

Fig. 20 Comparison of the OC1-y displacement response on mixed discrete-continuum and full deformable

with parameters $\boldsymbol{\theta} = \{A, \gamma, T_p, t_0, \varphi\}$: amplitude A, envelope width $\gamma > 1$, carrier period T_p, center time t_0, and phase φ. Over its support $t \in [t_0 - \gamma T_p/2,\ t_0 + \gamma T_p/2]$, the M&P pulse velocity is defined as Eq. (31) with closed-form expressions for $a_{MP}(t)$ and $u_{MP}(t)$ obtained by differentiation/integration.

$$v_{MP}(t) = \begin{cases} \dfrac{A}{2}\left[1 + \cos\left(\dfrac{2\pi}{\gamma T_p}(t - t_0)\right)\right] \cos\left(\dfrac{2\pi}{T_p}(t - t_0) + \varphi\right), & t_0 - \dfrac{\gamma T_p}{2} \le t \le t_0 + \dfrac{\gamma T_p}{2}, \\ 0, & \text{otherwise.} \end{cases} \tag{31}$$

The carrier period is fixed at the dominant spectral peak, $T_p = 0.526$ s. With ξ=0.05, the amplitude is scaled from the pseudo-spectral velocity at T_p as

$$A = \frac{4\,\xi\,\mathrm{PSV}(T_p)}{1 - e^{-2\pi\gamma\xi}}\left(1 + (\gamma - 1)\xi\right). \tag{32}$$

The remaining parameters are identified by maximizing the Pearson cross-correlation between $v_w(t)$ and the processed velocity $v(t)$ over bounded grids:

$$\gamma \in [1.01,\ 10]\ (100\ \text{samples}), \quad t_0 \in [0,\ 5]\ \text{s}\ (100\ \text{samples}), \quad \varphi \in [0,\ 396]\ (36\ \text{samples}).$$

Peak constraints are imposed to avoid unrealistic pulses:

$$|v_{MP}|_{\max} \le 26.33\ \text{cm/s}, \quad |a_{MP}|_{\max} \le 4.25\ \text{m/s}^2, \quad |u_{MP}|_{\max} \le 37\ \text{mm}.$$

The optimal $(\gamma^\star, t_0^\star, \varphi^\star)$ maximizes the correlation metric. The input window is the fitted pulse support $\left[t_0^\star - \frac{\gamma^\star T_p}{2},\ t_0^\star + \frac{\gamma^\star T_p}{2}\right]$, applied to the original AQA record. This compact, reproducible selection follows the practical wavelet-based truncation logic by Repapis et al. (2020).

Figures 21a and b show the extracted wavelet pulse overlaid on the original input and the resulting truncated seismic signal, respectively. Applying this method to the AQA earthquake record results in a reduced input duration of 4.34 s, spanning from 0.86 s to 5.20 s. For comparison, the significant duration method (Trifunac and Brady 1975), which uses the 10–90% Arias intensity range, yields an effective duration of 5.34 s (Bianchini et al. 2024a).

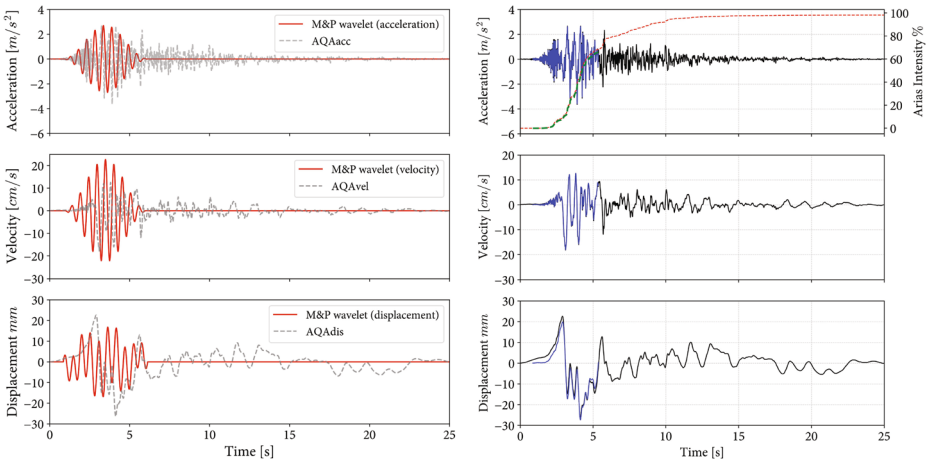

(a) Wavelet truncation method (b) Truncated AQA EQ

Fig. 21 Truncated AQA EQ record using the wavelet method by Repapis et al. (2020)

Figure 21b shows that the truncation method, with baseline correction, produced a coinciding acceleration and velocity response. Still, the displacement plot is slightly different from that of the original EQ record. Furthermore, the truncated seismic record accounts for Arias intensity increase from 0% to 70%. Even though the accounted Arias intensity is lower than the significant duration-based truncation method (Trifunac and Brady 1975), it can be seen in Fig. 21b that the truncation passed through both the maximum and minimum observed displacements. Considering that the wavelet-based truncation method is sufficiently accurate to predict both displacement peaks, this method is used in the dynamic analysis of the cross-vault model using Rayleigh damping.

6.2 Comparative analysis of numerical results

In this subsection, incremental dynamic analysis up to the truncated AQA75 record is conducted on the MassProp, Maxwell, noDamp, and Rayleigh models with the mixed discrete-continuum representation. The displacement prediction and computational resources needed to complete the analysis based on the newly truncated record are compared.

The displacement response of each damping scheme at the vault crown (OC1-y) using the modified model and record at each seismic load increment is given in Fig. 22. At AQA25, the experimental maximum and minimum peak displacements are predicted significantly well across all damping schemes, as no damage is found at this stage, both numerically and experimentally. At AQA50, the maximum and minimum peak displacements from all damping schemes underestimated the experimentally observed displacements, with averaged relative errors of 6.82% and 12.38% for the maximum and minimum peak displacements, respectively. The maximum displacement prediction error increased at 75% scaling with an average error of 11.63%, although the minimum peak displacement prediction error drops to 4.93%.

The relative error to EXP at AQA75 on each observed measurement point is summarized in Fig. 23. There are no significant differences in the prediction error on $OC2$ and $OC4$

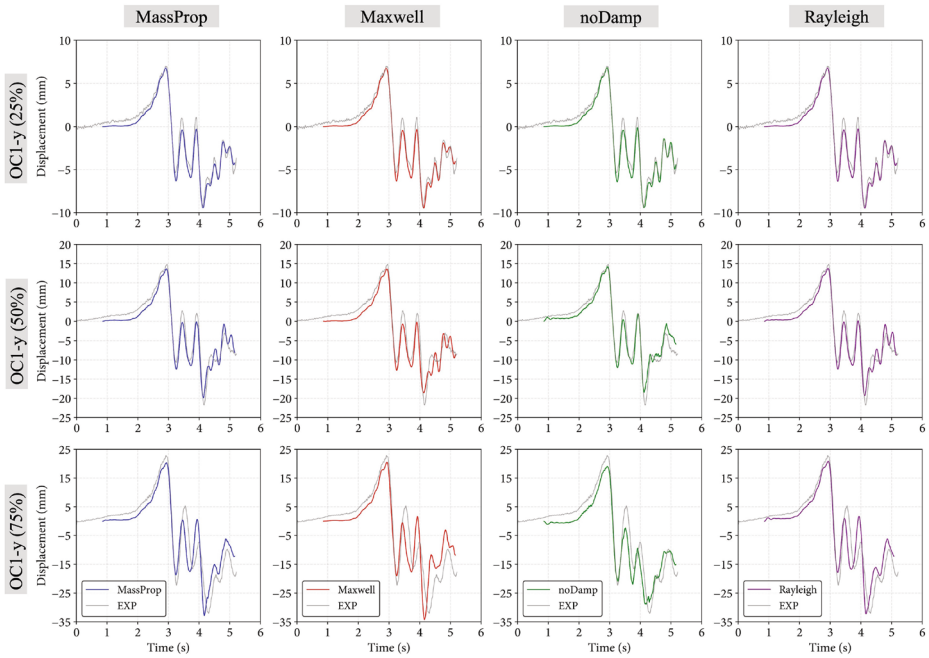

Fig. 22 The OC1-y displacement response prediction of each damping scheme using the modified model and truncated seismic record

across all compared damping schemes. The Rayleigh damping model predicts the maximum and minimum peak displacement at the crown vault relatively better than the other damping schemes. However, when the prediction error is compared to the model with the longer seismic record (Fig. 15), the OC1-y prediction error is relatively higher. This larger prediction error can be attributed to the truncation method, where the maximum peak displacement observed in the displacement history of the truncated EQ record (Fig. 21b) is lower than the full EQ record. Nevertheless, the truncation method coupled with the mixed-discrete continuum method to increase the target timestep is sufficiently capable of facilitating the dynamic analysis of complex structures using Rayleigh damping.

In this analysis with mixed-discrete block formulation, the dynamic timestep for each damping scheme has increased compared to the fully deformable model. The dynamic timesteps for the MassProp, Maxwell, noDamp, and Rayleigh models are 4.5×10^{-6} s, 3.75×10^{-6} s, 4.5×10^{-6} s, and 1.47×10^{-8} s, respectively. Using the same computational resource as the one used for Sect. 5, the entire incremental dynamic analysis (up to AQA75) for the MassProp and noDamp models took 3.5 hours to complete, while the Maxwell model took 6.25 hours to complete. However, the Rayleigh model took 1.5 months to complete the entire run, even with the newly truncated seismic record. This concludes that although using the full Rayleigh damping scheme provides only a slight gain in accuracy in terms of displacement prediction, it is shown to be prohibitive for a complex model such as the cross-vault.

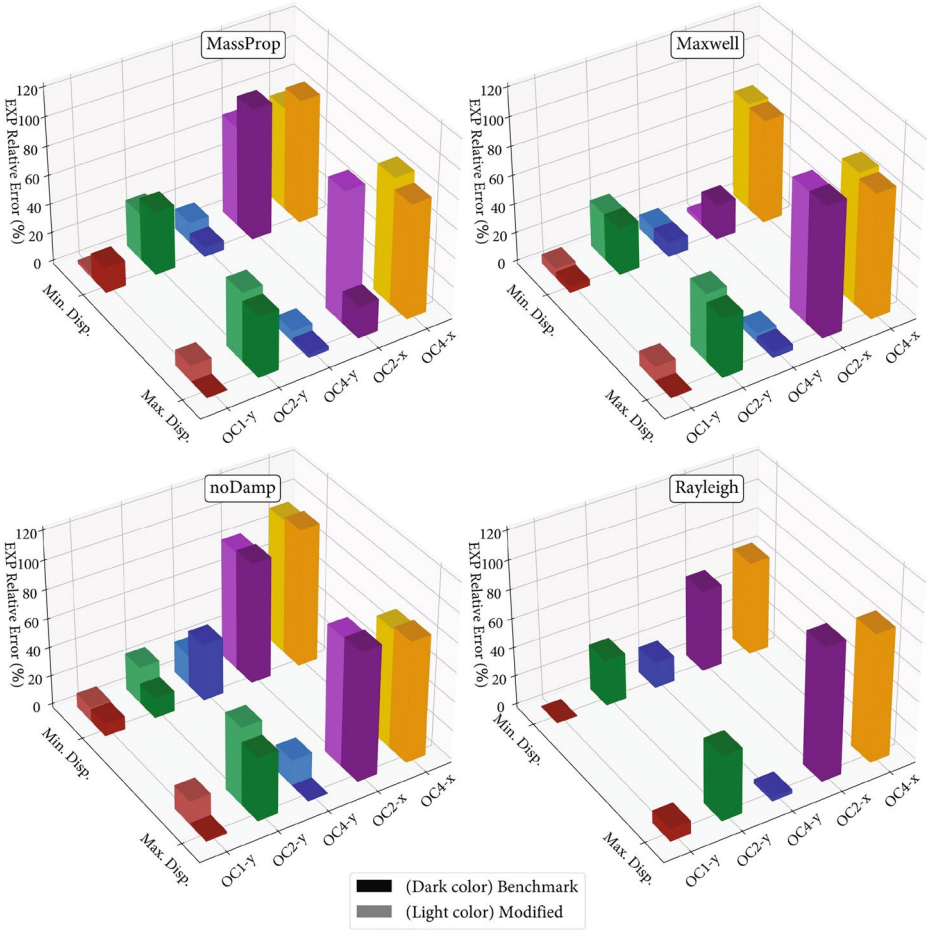

Fig. 23 Maximum and minimum peak displacement relative error to EXP of the modified model and truncated record at AQA75

7 Conclusions

This study presents a comprehensive evaluation of damping schemes for the dynamic analysis of unreinforced masonry (URM) cross-vaults, contributing significantly to the advancement of seismic assessment techniques using the Distinct Element Method (DEM). A novel implementation of Maxwell damping is introduced, accompanied by an optimisation framework that enables the automated tuning of multiple Maxwell elements to achieve a near-uniform damping ratio over a specified frequency range. This approach eliminates the reliance on heuristic calibration or trial-and-error procedures, offering a systematic method for damping characterisation in DEM.

The performance of the proposed Maxwell damping model is benchmarked against traditional approaches—mass-proportional damping and zero-viscous damping—using shake-table data from a URM cross-vault as reference. Due to the severe timestep constraints

and well-documented prohibitive computational cost associated with stiffness-proportional and Rayleigh damping models in explicit time integration schemes, these models were not included in the comparison.

Under the tested conditions, the Maxwell damping configuration showed modest, case-dependent improvements relative to the alternatives. It reduced peak displacement errors by 75 and 50% compared to the mass-proportional and zero-viscous models, respectively, and improved peak acceleration at crown-vault accuracy by 64 and 74%, while aiding numerical stability and reducing high-frequency noise. These benefits, however, came with an average 40% increase in computational time in our setup. Albeit this may be deemed as acceptable especially when performing a limited set of nonlinear dynamic analyses as commonly done when using discontinuum and in general advanced numerical models (typically 11 are recommended (Crowley et al. 2017)), further studies involving different structural types and sub-systems at different scales are needed to generalize the findings of this paper.

This study highlights the difficulties of using classical stiffness proportional relaxation methods in DEM and the necessity of modifications, such as adopting a mixed-discrete continuum approach and a wavelet-based trun-cation method, to address computational limitations. The mixed discrete-continuum approach adopted herein enhanced computational efficiency through partial density scaling with minimal impact on critical structural components, while the wavelet-based truncation method allowed for effective signal reduction, preserving reasonable accuracy in peak displacement predictions. The analyses conducted on the modified model revealed that the prohibitive computational costs outweigh the slight improvement in prediction accuracy offered by full Rayleigh damping.

Importantly, this work is the first to integrate Maxwell damping with an optimisation algorithm within a DEM framework for the dynamic analysis of large-scale URM cross-vaults. It marks a significant step forward from prior research by extending damping assessments beyond simplified rocking blocks to geometrically complex structural assemblies validated against experimental data. The methodology developed herein lays a foundation for systematic damping scheme comparisons in DEM, addressing both numerical and practical challenges.

In terms of future work and current limitations, it is worth mentioning that our study does not model complete collapse, focusing instead on the seismic load increments to structural failure. Subsequent work will select experimental campaigns that involve the full collapse of the structures to validate the performance of each damping scheme in extreme situations. Second, while this study focuses on masonry cross-vaults, future research should compare different damping schemes across different types of geometries, e.g., arches, domes, and low-to-mid-rise standard buildings, to generalize the findings. Finally, the current research only focuses on unreinforced masonry structures. Investigating different damping performances in the dynamic analysis of retrofitted masonry structures could provide insights into their effectiveness in preservation and retrofitting.

Author contributions All authors contributed to the study conception and design. Material preparation, data collection and analysis were performed by Y.P. Oktiovan, B. Pulatsu, and D. Malomo. The first author Y.P. Oktiovan implemented the optimisation framework in *3DEC* and performed the numerical simulations. The second author J. V. Lemos implemented the Maxwell damping scheme in *3DEC*. The first draft of the manuscript was written by Y.P. Oktiovan and all authors commented on previous versions of the manuscript. All authors read and approved the final manuscript.

Funding The authors declare that no funds, grants, or other support were received during the preparation of this manuscript.

Data availability The datasets generated during and/or analysed during the current study are available from the corresponding author, Y. P. Oktiovan, on reasonable request.

Declarations

Competing interests The authors have no relevant financial or non-financial interests to disclose.

References

Bathe KJ, Wilson EL (1976) Numerical methods in finite element analysis. Prentice-Hall civil engineering and mechanics series, Prentice-Hall. https://cir.nii.ac.jp/crid/1130282272328853376

Belytschko T (1983) An overview of semidiscretization and time integration procedures. Comput Methods Transient Anal 1–65

Belytschko T, Liu WK, Moran B et al (2013) Chapter 6 (solution methods and stability). In: Nonlinear finite elements for continua and structures, 2nd edn. John Wiley & Sons, Chichester, UK

Bertolesi E, Adam JM, Rinaudo P et al (2019) Research and practice on masonry cross vaults – a review. Eng Struct 180:67–88. https://doi.org/10.1016/J.ENGSTRUCT.2018.10.085

Bianchini N, Mendes N, Calderini C et al (2024a) Shaking table testing of an unstrengthened and strengthened with textile reinforced mortar (TRM) full-scale masonry cross vault. Int J Archit Herit 1–26. https://doi.org/10.1080/15583058.2023.2295900

Bianchini N, Mendes N, Lourenço PB et al (2024b) Modelling of the dynamic response of a full-scale masonry groin vault: unstrengthened and strengthened with textile-reinforced mortar (TRM). Int J Archit Herit 1–25. https://doi.org/10.1080/15583058.2024.2320857

Bland DR (2016) The theory of linear viscoelasticity. Courier Dover Publications

Brandonisio G, Lucibello G, Mele E et al (2013) Damage and performance evaluation of masonry churches in the 2009 L'Aquila earthquake. Eng Fail Anal 34:693–714. https://doi.org/10.1016/J.ENGFAILANAL.2013.01.021

Calderini C, Bianchini N, Lourenço PB et al (2024) Shake-table testing of a brick masonry groin vault: overview of blind predictions and postdictions and comparison with experimental results. Int J Archit Herit 1–27. https://doi.org/10.1080/15583058.2024.2419545

CEBFIP1990 (1993) CEB-FIP model code 1990 for concrete structures. Comité euro-International du Béton / Fédération Internationale du Béton, Lausanne, Switzerland, source of empirical fracture-energy relations adopted by many masonry models by analogy

CEN (2004) EN 1998-1:2004 eurocode 8: design of structures for earthquake resistance – part 1: general rules, seismic actions and rules for buildings. European Committee for Standardization, Brussels, including amendments A1:2013 and corrigendum AC:2009

Chen S, Bagi K (2024) DEM analysis of the mechanical role of backfill of jointed masonry fan vaults: results of virtual experiments. Int J Archit Herit 18(1):64–83. https://doi.org/10.1080/15583058.2022.2104142

Chen S, Ferrante A, Clementi F et al (2021) DEM analysis of the effect of bond pattern on the load bearing capacity of barrel vaults under vertical loads. Int J Masonry Res Innov 6(3):346–373. https://doi.org/10.1504/IJMRI.2021.116234

Chopra AK (2017) Dynamics of structures: theory and applications to earthquake Engineering, 5th edn edn. Pearson, Harlow

Cole GL, Dhakal RP, Turner FM (2012) Building pounding damage observed in the 2011 Christchurch earthquake. Earthq Eng Struct Dyn 41(5):893–913. https://doi.org/10.1002/eqe.1164

Crowley H, Polidoro B, Pinho R et al (2017) Framework for developing fragility and consequence models for local personal risk. Earthq Spectra 33(4):1325–1345. https://doi.org/10.1193/083116eqs140m

Cundall PA (1988) Formulation of a three-dimensional distinct element model—part I. A scheme to detect and represent contacts in a system composed of many polyhedral blocks. Int J Rock Mech 25(3):107–116. https://doi.org/10.1016/0148-9062(88)92293-0

D'Altri AM, Castellazzi G, de Miranda S et al (2017) Seismic-induced damage in historical masonry vaults: a case-study in the 2012 emilia earthquake-stricken area. J Build Eng 13:224–243. https://doi.org/10.1016/J.JOBE.2017.08.005

Davis L, Cogliano M, Casotto C et al (2023) Pragmatic seismic collapse meso-scale analysis of old Dutch masonry churches. Earthq Eng Struct Dyn 53:622–645. https://doi.org/10.1002/EQE.4037

Dawson EM, Cheng Z (2021) Maxwell damping: an alternative to rayleigh damping. In: Geo-Extreme 2021, Geo-Extreme 2021. ASCE, pp 34–45. https://doi.org/10.1061/9780784483701.004

de Felice G, Liberatore D, De Santis S et al (2022) Seismic behaviour of rubble masonry: shake table test and numerical modelling. Earthq Eng Struct Dyn 51(5):1245–1266. https://doi.org/10.1002/EQE.3613

De Lorenzis L, DeJong M, Ochsendorf J (2007) Failure of masonry arches under impulse base motion. Earthq Eng Struct Dyn 36(14):2119–2136. https://doi.org/10.1002/EQE.719

DeJong MJ (2009) Seismic assessment strategies for masonry structures. Doctoral thesis, Massachusetts Institute of Technology, 77 Massachusetts Avenue Cambridge, MA 02139-4307

Dell'endice A, Iannuzzo A, DeJong MJ et al (2021) Modelling imperfections in unreinforced masonry structures: discrete element simulations and scale model experiments of a pavilion vault. Eng Struct 228:111499. https://doi.org/10.1016/J.ENGSTRUCT.2020.111499

Ferrante A, Dubois F, Morenon P (2024) Comparison of continuous and discrete modeling strategies for the structural assessment of a masonry vault under dynamic seismic loading. Int J Archit Herit. https://doi.org/10.1080/15583058.2024.2377297

Findley WN, Davis FA (2013) Creep and relaxation of nonlinear viscoelastic materials. Courier Dover Publications

Galvez F, Dizhur D, Ingham JM (2023) Adjacent interacting masonry structures: shake table test blind prediction discrete element method simulation. Bull Earthq Eng 22(12):6037–6063. https://doi.org/10.1007/S10518-023-01640-Y/FIGURES/16

Galvez F, Sorrentino L, Dizhur D et al (2022a) Damping considerations for rocking block dynamics using the discrete element method. Earthq Eng Struct Dyn 51(4):935–957. https://doi.org/10.1002/EQE.3598

Galvez F, Sorrentino L, Dizhur D et al (2022b) Seismic rocking simulation of unreinforced masonry parapets and façades using the discrete element method. Earthq Eng Struct Dyn 51(8):1840–1856. https://doi.org/10.1002/EQE.3641

Genta G (2009) Vibration dynamics and control, vol 616. Springer, New York

Godio M, Beyer K (2019) Evaluation of force-based and displacement-based out-of-plane seismic assessment methods for unreinforced masonry walls through refined model simulations. Earthq Eng Struct Dyn 48(4):454–475. https://doi.org/10.1002/EQE.3144

Gubana A, Melotto M (2021) Evaluation of timber floor in-plane retrofitting interventions on the seismic response of masonry structures by DEM analysis: a case study. Bull Earthq Eng 19(14):6003–6026. https://doi.org/10.1007/S10518-021-01190-1/FIGURES/13

Hall JF (2006) Problems encountered from the use (or misuse) of Rayleigh damping. Earthq Eng Struct Dyn 35(5):525–545. https://doi.org/10.1002/EQE.541

Huang Y, Sturt R, Willford M (2019) A damping model for nonlinear dynamic analysis providing uniform damping over a frequency range. Comput Struct 212:101–109. https://doi.org/10.1016/j.compstruc.2018.10.016

Iannuzzo A, Dell'endice A, Avelino R et al (2021) COMPAS masonry: a computational framework for practical assessment of unreinforced masonry structures. In Proceedings of the 12th International Conference on Structural Analysis of Historical Constructions (SAHC 2020), SAHC, Barcelona, 1882–1892. https://doi.org/10.23967/sahc.2021.054

Itasca Consulting Group Inc (2013) 3DEC - Three dimensional distinct element code ver. 7.0. Software

Kim J, Lorenzoni F, Salvalaggio M et al (2021) Seismic vulnerability assessment of free-standing massive masonry columns by the 3D discrete element method. Eng Struct 246:113004. https://doi.org/10.1016/J.ENGSTRUCT.2021.113004

Lagomarsino S (2012) Damage assessment of churches after L'Aquila earthquake (2009). Bull Earthq Eng 10:73–92. https://doi.org/10.1007/s10518-011-9307-x

Lemos J (2008) Block modelling of rock masses: concepts and application to dam foundations. Eur J Environ Civ Eng 12(7–8):915–949

Lemos J, Sarhosis V (2023) Dynamic analysis of masonry arches using Maxwell damping. Struct 49:583–592. https://doi.org/10.1016/j.istruc.2023.01.139

Lemos JV, Dawson E, Cheng Z (2022) Application of Maxwell damping in the dynamic analysis of masonry structures with discrete elements. Int J Masonry Res Innov 7(6):663–686. https://doi.org/10.1504/ijmri.2021.10043266

Liu HP, Anderson DL, Kanamori H (1976) Velocity dispersion due to anelasticity; implications for seismology and mantle composition. Geophys J Int 47(1):41–58. https://doi.org/10.1111/j.1365-246X.1976.tb01261.x

Lourenço PB (1996) Computational strategies for masonry structures. Doctoral thesis, Delft University, Stevinweg 1, 2628CN Delft, NL

Lourenço PB (2010) Recent advances in masonry modelling: micromodelling and homogenisation. Multiscale Modeling in Solid Mechanics: Computational Approaches pp 251–294

Lourenço PB, Rots JG (1997) Multisurface interface model for analysis of masonry structures. J Eng Mech 123(7):660–668. https://doi.org/10.1061/(ASCE)0733-9399(1997)123:7(660)

Malomo D, DeJong MJ (2022) M-DEM simulation of seismic pounding between adjacent masonry structures. Bull Earthq Eng 1–26. https://doi.org/10.1007/S10518-022-01545-2/FIGURES/12

Malomo D, DeJong MJ, Penna A (2019) Distinct element modelling of the in-plane cyclic response of URM walls subjected to shear-compression. Earthq Eng Struct Dyn 48(12):1322–1344. https://doi.org/10.1002/eqe.3178

Malomo D, Pulatsu B (2024) Discontinuum models for the structural and seismic assessment of unreinforced masonry structures: a critical appraisal. Struct 62:106108. https://doi.org/10.1016/J.ISTRUC.2024.106108

Masi F, Stefanou I, Maffi-Berthier V et al (2020) A discrete element method based-approach for arched masonry structures under blast loads. Eng Struct 216:110721. https://doi.org/10.1016/J.ENGSTRUCT.2020.110721

Mavroeidis GP, Dong G, Papageorgiou AS (2004) Near-fault ground motions, and the response of elastic and inelastic single-degree-of-freedom (SDOF) systems. Earthq Eng Struct Dyn 33(9):1023–1049. https://doi.org/10.1002/EQE.391

Mele T, Mcinerney J, DeJong M et al (2012) Physical and computational discrete modeling of masonry vault collapse. In Proceedings of the 8th International Conference on Structural Analysis of Historical Constructions

Meriggi P, De Felice G, De Santis S et al (2019) Distinct element modelling of masonry walls under out-of-plane seismic loading. Int J Archit Herit 13(7):1110–1123. https://doi.org/10.1080/15583058.2019.1615152

Oktiovan Y, Messali F, Rots J (2023a) Detailed distinct element modeling of a utrecht wharf cellar for the assessment of the load-bearing capacity and failure mechanism. In Proceedings of the Seventeenth International Conference on Civil, Structural and Environmental Engineering Computing 6, pp 1–10. https://doi.org/10.4203/CCC.6.6.2

Oktiovan YP, Davis L, Wilson R et al (2023b) Simplified micro-modeling of a masonry cross-vault for seismic assessment using the Distinct element method. Int J Archit Herit. https://doi.org/10.1080/15583058.2023.2277328

Oktiovan YP, Messali F, Pulatsu B et al (2024) A contact-based constitutive model for the numerical analysis of masonry structures using the distinct element method. Comput Struct 303:107499. https://doi.org/10.1016/J.COMPSTRUC.2024.107499

Paris V, Pizzigoni A, Adriaenssens S (2020) Statics of self-balancing masonry domes constructed with a cross-herringbone spiraling pattern. Eng Struct 215:110440. https://doi.org/10.1016/J.ENGSTRUCT.2020.110440

Peña F, Prieto F, Lourenço PB et al (2007) On the dynamics of rocking motion of single rigid-block structures. Earthq Eng Struct Dyn 36(15):2383–2399. https://doi.org/10.1002/EQE.739

Pulatsu B (2023) Coupled elasto-softening contact models in DEM to predict the in-plane response of masonry walls. Comput Part Mech 10:1759–1770. https://doi.org/10.1007/s40571-023-00586-x

Pulatsu B, Erdogmus E, Lourenço PB (2019) Comparison of in-plane and out-of-plane failure modes of masonry arch bridges using discontinuum analysis. Eng Struct 178:24–36. https://doi.org/10.1016/J.ENGSTRUCT.2018.10.016

Pulatsu B, Erdogmus E, Lourenço PB et al (2020) Simulation of the in-plane structural behavior of unreinforced masonry walls and buildings using DEM. Struct 27:2274–2287. https://doi.org/10.1016/J.ISTRUC.2020.08.026

Repapis CC, Mimoglou PP, Dimakopoulou VV et al (2020) Efficient strong motion duration of pulse-like records for nonlinear structural analyses. Earthq Eng Struct Dyn 49(5):479–497. https://doi.org/10.1002/EQE.3249

Sarhosis V, Oliveira DV, Lemos JV et al (2014) The effect of skew angle on the mechanical behaviour of masonry arches. Mech Res Commun 61:53–59. https://doi.org/10.1016/J.MECHRESCOM.2014.07.008

Smoljanović H, Živaljić N, N (2013) A combined finite-discrete element analysis of dry stone masonry structures. Eng Struct 52:89–100. https://doi.org/10.1016/j.engstruct.2013.02.010
Sorrentino L, Liberatore L, Decanini LD et al (2014) The performance of churches in the 2012 emilia earthquakes. Bull Earthq Eng 12(5):2299–2331. https://doi.org/10.1007/s10518-013-9519-3
Tomassetti U, Graziotti F, Sorrentino L et al (2019) Modelling rocking response via equivalent viscous damping. Earthq Eng Struct Dyn 48(11):1277–1296. https://doi.org/10.1002/EQE.3182
Trifunac MD, Brady AG (1975) A study on the duration of strong earthquake ground motion. Bull Seismol Soc Am 65(3):581–626. https://doi.org/10.1785/BSSA0650030581

Authors and Affiliations

Yopi P. Oktiovan[1] · José V. Lemos[2] · Bora Pulatsu[3] · Francesco Messali[1] · Jan G. Rots[1] · Daniele Malomo[4]

✉ Yopi P. Oktiovan
y.p.oktiovan@tudelft.nl

[1] Faculty of Civil Engineering and Geosciences, Delft University of Technology, Delft, Netherlands

[2] National Laboratory for Civil Engineering (LNEC), Lisbon, Portugal

[3] Department of Civil and Environmental Engineering, Carleton University, Ottawa, Canada

[4] Department of Civil Engineering, McGill University, Montréal, Canada